

AD-A118 459

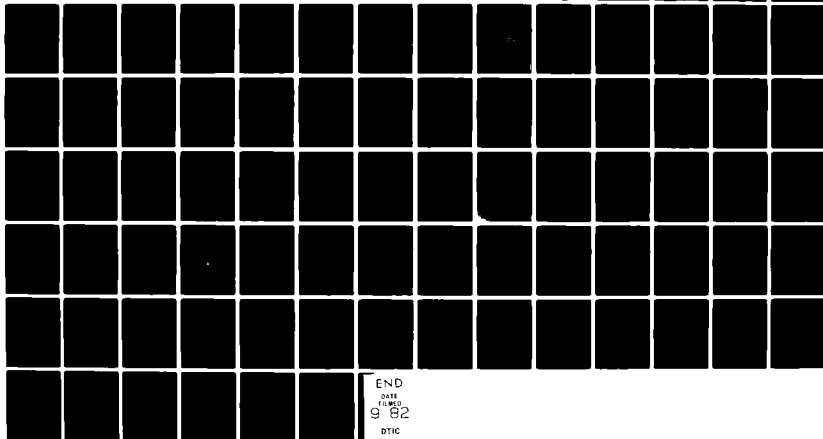
MCDONNELL DOUGLAS RESEARCH LABS ST LOUIS MO F/G 12/1  
ALGORITHM FOR SURFACE OF TRANSLATION ATTACHED RADIATORS (A-STAR--ETC(U)  
MAY 82 L N MEDGYESI-MITSCHANG, J M PUTNAM F30602-80-C-0106

UNCLASSIFIED

RADC-TR-82-113-VOL-1

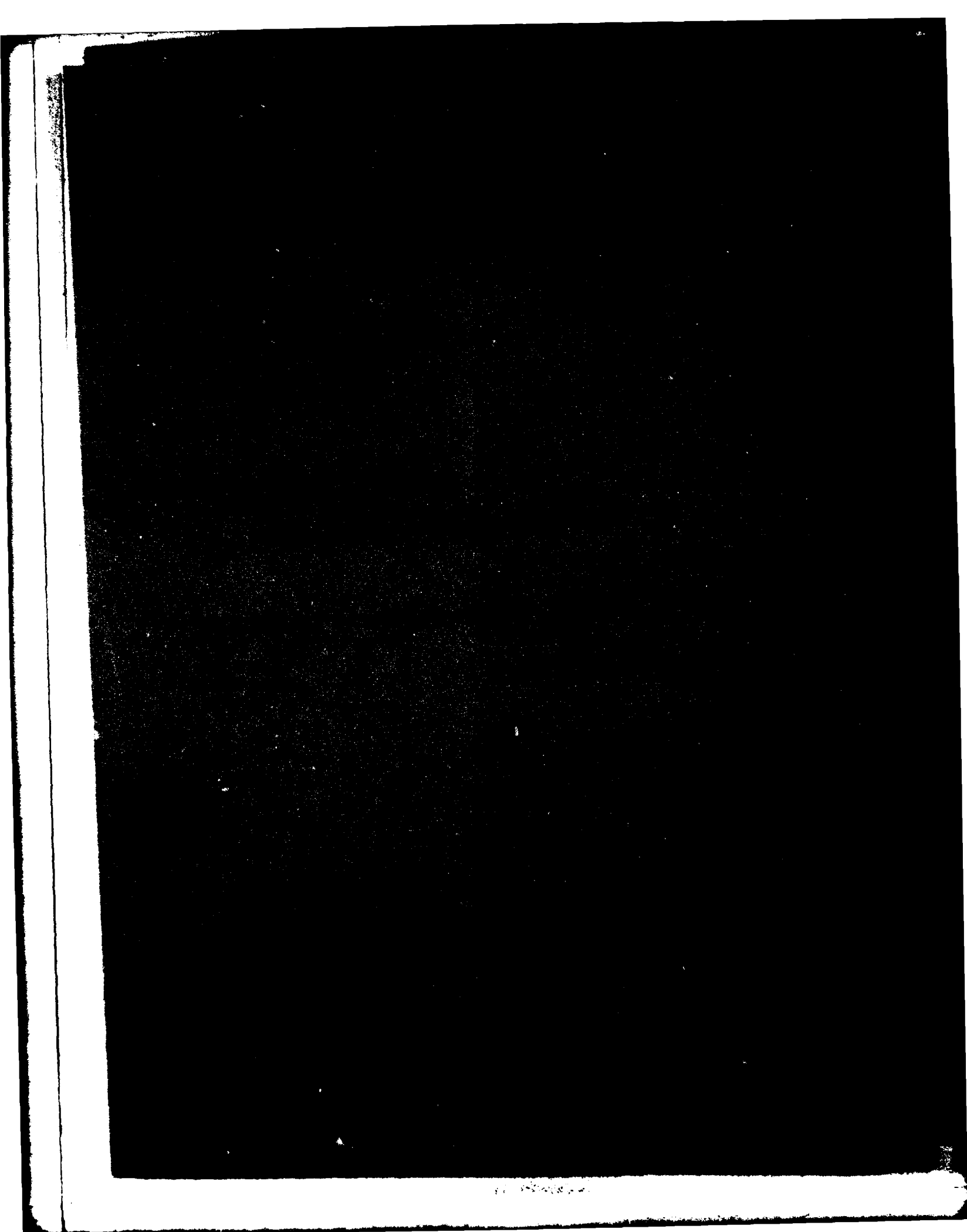
NL

1-1  
AD-A118 459



END  
DATE  
FILMED  
9 82  
DTIC

AD A118459



SECURITY CLASSIFICATION OF THIS PAGE (When Data Entered)

DD FORM 1 JAN 73 1473 EDITION OF 1 NOV 65 IS OBSOLETE

**SECURITY CLASSIFICATION OF THIS PAGE (When Data Entered)**

**UNCLASSIFIED**

**SECURITY CLASSIFICATION OF THIS PAGE(When Data Entered)**

consideration is given to the attachment point of wire antennas on the BOT. The theoretical development parallels in part the MM formulation developed earlier for bodies of revolution (BOR) and BOR with wire radiators. A modal expansion is used to describe the unknown surface currents on the BOT. The analysis treats the far-field radiation and scattering from a BOT excited by active antennas or illuminated by a plane wave of arbitrary polarization and angle of incidence. In addition, electric and magnetic near-field and coupling analyses of active wire and aperture (slot) antennas are developed. The entire formulation has been implemented by the A-STAR computer algorithm and validated using accepted data in the literature. The user/systems manual (Volume II) provides a detailed description of the use of the codes and example problems. Program listings are given in Volume III.

**UNCLASSIFIED**

**SECURITY CLASSIFICATION OF THIS PAGE(When Data Entered)**

# TABLE OF CONTENTS

	<u>Page</u>
1. INTRODUCTION AND BACKGROUND.....	1
2. SUMMARY OF COMPLETED EFFORT.....	3
3. SUMMARY OF PREVIOUS WORK.....	5
4. GENERALIZED MM/BOT FORMULATION.....	7
4.1 Electric-Field Integral Equation.....	9
4.2 Basis Functions for the Currents.....	10
4.3 Impedance Expressions.....	12
4.3.1 Junction-Independent Impedance Matrices.....	15
4.3.2 Junction-Dependent Impedance Matrices.....	18
4.3.3 Edge-Dependent Impedance Matrices.....	20
4.4 General Structures and Properties of the $Z_{BOT}$ Matrix.....	21
5. FAR-FIELD RADIATION AND SCATTERING ANALYSIS.....	24
5.1 Embedded Antennas.....	29
5.2 Off-Surface Radiators.....	32
5.3 Scattered Fields.....	32
6. NEAR-FIELD AND ANTENNA COUPLING ANALYSIS.....	34
6.1 Electric Near-Field Formulation.....	34
6.2 Magnetic Near-Field Formulation.....	38
6.3 Coupling Analysis.....	41
7. VALIDATION AND APPLICATION OF THE GENERALIZED MM/BOT FORMULATION.....	43
7.1 Validation of the Far-Field Analysis.....	43
7.1.1 Embedded (Slot) Antennas.....	43
7.1.2 Off-Surface Antennas.....	45
7.2 Validation of the Scattering Analysis.....	50
7.3 Validation of Near-Field Analysis.....	52
8. COMPUTER IMPLEMENTATION.....	59
APPENDIX A: DERIVATION OF THE IMPEDANCE MATRICES.....	60
A.1 Impedance Matrix for the BOT Surface, $Z_{mn}^{ss}$ .....	60
A.2 Impedance Matrix for the Caps, $Z^{cc}$ .....	64
A.3 Impedance Matrix for the BOT-Cap Interactions, $Z_m^{sc}$ .....	66
A.4 Impedance Matrix for the BOT-Wire Interactions, $Z_m^{sw}$ .....	68

# TABLE OF CONTENTS (Continued)

	<u>Page</u>
A.5 Impedance Matrix for the Cap-Wire Interactions, $Z^{CW}$ .....	69
A.6 BOT-Junction Impedance Matrix, $Z_m^{sj}$ .....	70
A.7 Edge-Dependent Impedance Matrices.....	72
REFERENCES.....	76

# LIST OF ILLUSTRATIONS

<u>Figure</u>	<u>Page</u>
1. BOT-wire/antenna configurations.....	2
2. Generic BOT-wire geometry.....	7
3. Detail of cap coordinate geometry.....	11
4. Detail of edge region.....	12
5. Structure of $Z_{BOT}$ matrix.....	22
6. Coordinate geometry for transfer matrix evaluation on BOT....	25
7. Slotted cylinder geometry.....	44
8. Comparison of MM/BOR and MM/BOT computed power radiation patterns: slotted cylinder.....	44
9. Comparison of MM/BOR and MM/BOT computed power radiation patterns: cylinder-mounted monopole.....	46
10. Comparison of MM/BOR and MM/BOT computed power radiation patterns: cylinder-mounted opposing monopoles (active and passive).....	47
11. Comparison of MM/BOR and MM/BOT computed power radiation patterns with experiment: cylinder-mounted active and passive monopoles.....	48
12. Power radiation patterns for wing-mounted monopoles.....	49
13. Comparison of MM/BOR and MM/BOT computed bistatic cross section for open cylinder.....	50
14. Measured and predicted monostatic cross section for capped cylinder.....	51
15. Measured and predicted monostatic cross section for a square plate.....	52
16. Comparison of MM/BOR and MM/BOT calculated bistatic cross section for a thin conducting disk.....	53
17. Classical solution for slit cylinder ( $\phi$ -excited slit) .....	54
18. Computation of near fields for slit cylinder at $\phi = 0$ (slit angle = $45^\circ$ ).....	55
19. Computation of near fields for slit cylinder at $\phi = 45^\circ$ (slit angle = $45^\circ$ ).....	56



LIST OF ILLUSTRATIONS (Continued)

<u>Figure</u>	<u>Page</u>
20. Computation of near fields for slit cylinder at $\phi = 90^\circ$ (slit angle = $45^\circ$ ).....	57
21. Near fields for wing-mounted monopoles.....	58

## LIST OF TABLES

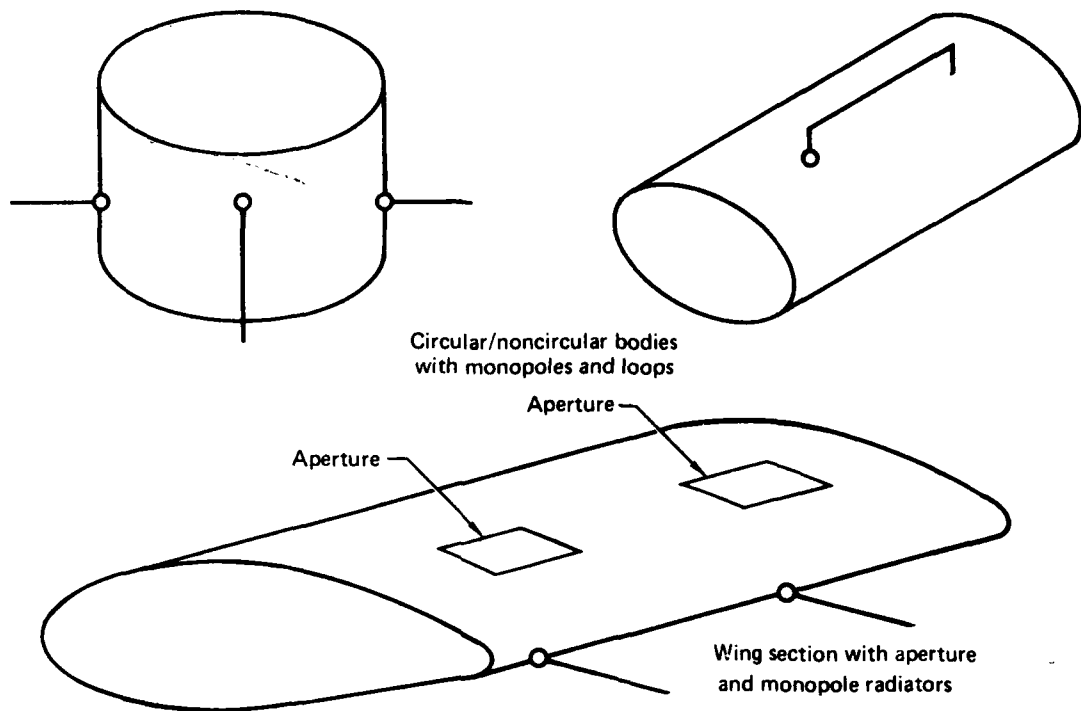
<u>Table</u>	<u>Page</u>
1. Junction and Wire Impedance Elements.....	18
2. Transfer Matrix Elements.....	26

## 1. INTRODUCTION AND BACKGROUND

This report describes a formulation developed for analysis of radiation from slot antennas and off-surface wire radiators on open or closed asymmetric bodies, denoted here as bodies of translation (BOT). Representative examples of such configurations are shown in Figure 1. The case of near-fields in the vicinity of such antennas is treated as a subcase. The formulation, based on the method of moments (MM), is a generalization of the results given in References 1-3. The computer algorithm A-STAR (Algorithm for Surface of Translation Attached Radiators) implements this analysis and is described in detail in Vol. II of this report. The listing of the codes is given in Vol. III.

The MM technique has been applied to a plethora of electromagnetic problems that are associated with complex aerospace systems. Generally, the classical partial differential equation formulations of such problems are analytically and computationally intractable. On the other hand, the equivalent electric- or magnetic-field integral equation (EFIE or MFIE) formulations of these cases are often amenable to solution by the MM approach. In these integral formulations, the radiating or scattering structures and surfaces can be represented by wires, surface patches, or wire grids.<sup>1,3,4,5</sup> The computational requirements of the method to date have limited application of these methods to bodies with surface areas on the order of a few square wavelengths ( $\lambda^2$ ). Larger surfaces (of  $\sim 45\lambda^2$ ) can be analyzed via the MM technique if the vehicle body has some degree of symmetry, such as in the case of bodies of revolution (BOR). The present analytical technique, denoted as MM/BOT, combines many of the computationally cost-effective features of the MM/BOR analysis<sup>5</sup> with some of the shape flexibility of the wire-grid approach.<sup>6</sup> This combination permits treatment of difficult boundary conditions associated with realistic radiating and scattering geometries, such as parts of wing sections or noncircular aircraft fuselages with attached or embedded antennas.

### Asymmetric Surfaces - Radiation Analysis



### Asymmetric Surfaces - Scattering Analysis

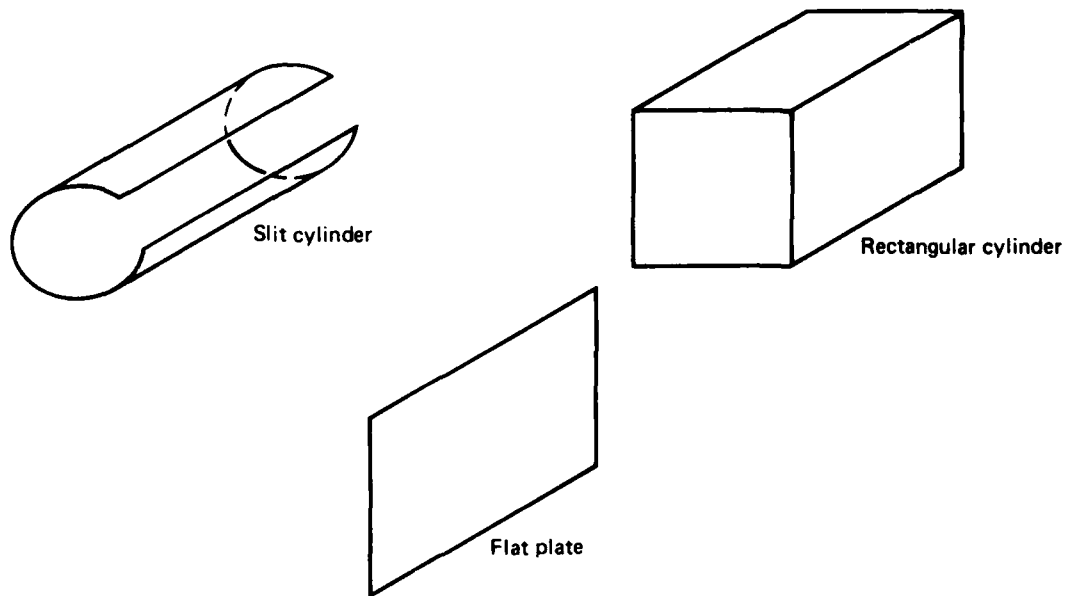


Figure 1. Body of translation (BOT) configurations.

## 2. SUMMARY OF COMPLETED EFFORT

The principal results of the completed effort are summarized below.

Detailed discussions of individual topics are given in the sections indicated.

- The MM/BOT formulation was developed for a general BOT configuration to treat the radiation from asymmetric aperture (slot) antennas and off-surface radiators (Sections 4 and 5). For radiating apertures, the formulation allows arbitrary polarization and antenna excitation to be specified. The results are shown to be in agreement with the predictions of the MM/BOR analysis<sup>5</sup> and with experimental measurements for wire antennas on surfaces of revolution.<sup>3</sup>
- The MM/BOT formulation was specialized to compute all electric and magnetic near-field components at an arbitrary point in the vicinity of a radiating or scattering BOT surface (Section 6). The coupling between wire and aperture antennas was treated (Section 6).
- The computer algorithm A-STAR was developed to implement all aspects of the MM/BOT formulation. The codes, written in FORTRAN IV, are modular, machine independent, and user oriented. All parts of the codes were tested, validated (Section 7), and installed on the RADC computer system. A user/systems manual (Volume II of this report) describes in detail the workings of the algorithm. A series of example problems is provided to illustrate the computational procedure for the prospective user.

The foregoing results have special relevance to RADC in the following areas:

- The generalized MM/BOT formulation allows efficient representation of asymmetric surfaces, such as wing sections and noncircular parts of aircraft fuselages, for electromagnetic analysis.
- The analysis models both aperture and off-surface wire antennas located on modern aircraft. Antenna radiation patterns can be computed efficiently for all polarizations.
- The near-field analysis allows the mapping of fields and currents in the neighborhood of radiators. The coupling analysis allows engineering criteria to be developed for suitable antenna placement on aircraft surfaces.

- The formulation demonstrates hybridizing of surface, wire, and patch modeling techniques in a consistent analytical framework leading to maximum computational flexibility for EM problems. This framework is adaptable to other EM codes developed by RADC such as GEMACS (General Electromagnetic Model for the Analysis of Complex Systems).

### 3. SUMMARY OF PREVIOUS WORK

The earliest application of the method of moments (MM) was for the analysis of thin-wire radiators and scatterers.<sup>7-8</sup> Recent investigators<sup>3,9-15</sup> have used the MM technique to examine such radiators on or near bodies of revolution (BOR). In many real-world situations involving aircraft and spacecraft, the principal physical features of the antenna platform adjacent to the antenna feed point often can be modeled as a BOR. Often the electrical size of the body to which the antenna is attached is comparable to a few wavelengths ( $\lambda$ ). In these cases, the entire structure is coupled closely to the antenna elements, so the whole configuration becomes a radiator. To analyze such configurations requires incorporation of complex boundary conditions in the electromagnetic formulation used. The MM technique is the most appropriate analytical tool for such problems.

To extend the usefulness of the MM analysis for a broader class of radiating geometries, we developed a MM formulation for antennas attached to, near to, or embedded in bodies of translation (BOT). Subcases of such surfaces are finite cylindrical bodies of arbitrary cross section, which can be open or closed. Previously, a MM formulation was used to treat asymmetric bodies using a wire representation for the surface.<sup>16</sup> However, the computer resources necessary to carry out the latter analysis are often prohibitive and limit its general use. In our formulation, an efficient analytical treatment is obtained allowing substantial configurational flexibility for both the antennas and the surfaces on which they are located. The theoretical development parallels in part the MM/BOR and MM/BOR-wire formulations in References 5 and 3 and retains the modal expansion concept for the currents on the surface.

The primary motivation for our investigation was the efficient analytical treatment of antennas on or near BOTs. The results of this work are easily extended to the scattering from such configurations. (For examples of the MM/BOR-wire formulation applied to scattering, see Reference 17.) Earlier investigators, such as Andreasen,<sup>18</sup> Wallenberg and Harrington,<sup>19</sup> and Wilton and Mittra,<sup>20</sup> primarily addressed the scattering from cylinders of arbitrary cross section and infinite length. The case of finite-length cylinders of

arbitrary cross sections has not been treated previously. Several investigators examined the special case of finite-length, right-circular cylinders for various limiting cases. For example, Ufimtsev,<sup>21</sup> Kieburts,<sup>22</sup> and Fialkovskii<sup>23</sup> developed solutions for thin cylinders with  $ka \ll 1$ , while Adey<sup>24</sup> considered long cylinders with  $ka = 1$ , where  $ka = 2\pi a/\lambda$  and  $a$  is the cylinder radius. Williams<sup>25</sup> studied the diffraction from finite-length, hollow cylinders where the open ends did not materially influence the diffracted waves. A complete study of tubular cylinders was made by Kao<sup>26,27</sup> for arbitrary length and  $ka$ , but it was restricted to broadside illumination. His formulation resulted in a pair of decoupled integral equations that was solved to yield the axial and the circumferential currents on the cylinder. Recently, Davis and Mittra<sup>28</sup> examined the current distribution on an open cylinder of  $l\lambda$  length and  $ka = 1$  using a hybrid formulation incorporating the EFIE and MFIE representations of Maxwell's equations. The present MM/BOT formulation treats the foregoing problems as special subcases.



#### 4. GENERALIZED MM/BOT FORMULATION

In the following analysis, as in Reference 1, the electromagnetic radiated or scattered fields are expressed in terms of potentials from which a general integral equation for the surface currents on the radiating or scattering body can be obtained. For maximum generality and unity of treatment, the EFIE formulation is chosen over the MFIE formulation for the currents on both the off-surface wire radiators and the BOT surface. The generic configuration addressed here is shown in Figure 2. The overall (closed) body is composed of a surface formed by an arbitrary generating curve translated along the  $z$ -axis, denoted as the BOT. The BOT can be terminated by planar end-caps with tangents normal to the  $z$ -axis. The assumption of a closed surface and planar caps is introduced to simplify the subsequent discussion and can be removed if desired. The vicinity of the antenna attachment point (Figure 2) is designated as the junction region, consisting a small annular disk on the BOT and a wire attachment segment on the antenna nearest the BOT surface.

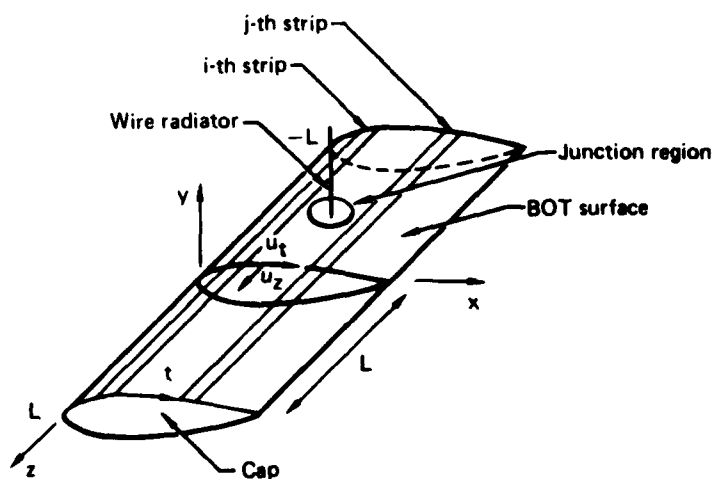


Figure 2 Generic BOT-wire configuration.

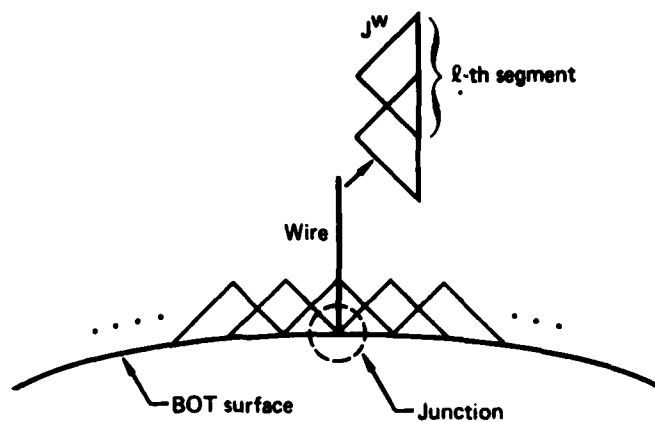


Figure 2a. Enlargement of BOT-wire attachment region

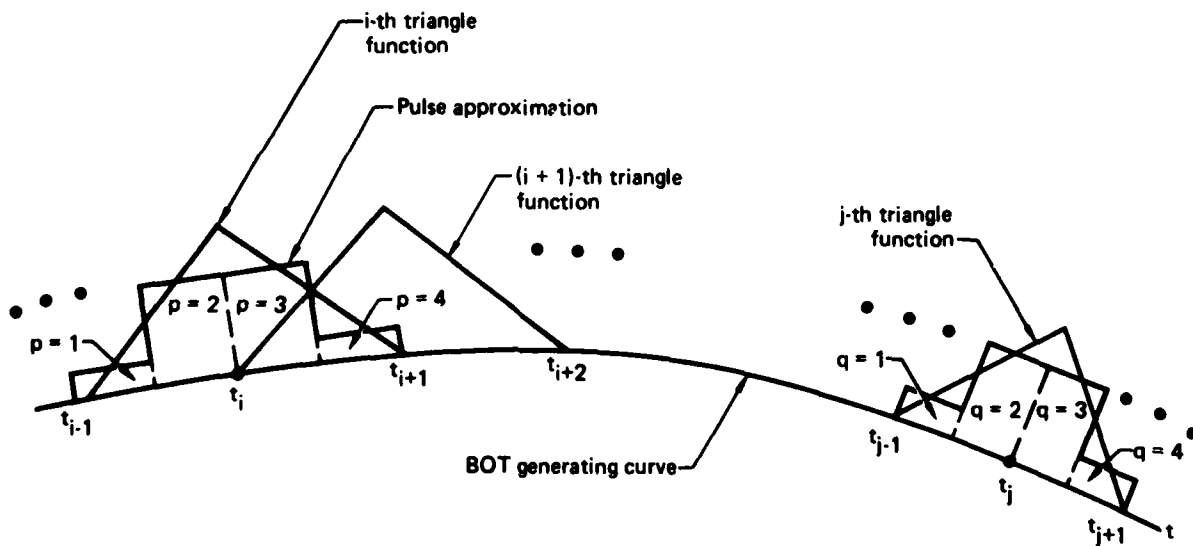


Figure 2b. Detail of pulse approximation for triangle function on BOT surface.

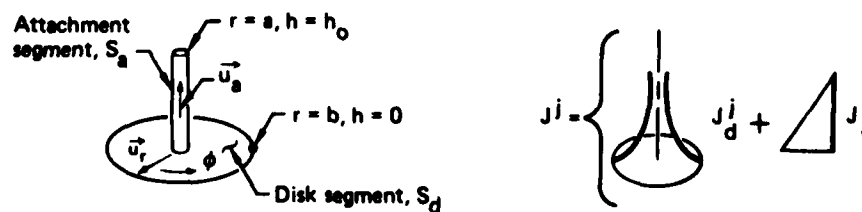


Figure 2c. Detail of junction region representation.

#### 4.1 Electric-Field Integral Equation

Imposing the usual boundary conditions on the perfectly conducting surfaces in Figure 2, the generalized EFIE expressed in terms of integro-differential operators  $L(\cdot)$  on the BOT, caps, wire, junction, and edge region is given by

$$(\vec{E}^i)_{\text{tan}} = -(\vec{E}^s)_{\text{tan}} = L_s(\vec{J}) + L_c(\vec{J}) + L_w(\vec{J}) + L_j(\vec{J}) + L_e(\vec{J}) , \quad (1)$$

where  $(\vec{E}^i)_{\text{tan}}$  and  $(\vec{E}^s)_{\text{tan}}$  denote the tangential components of the impressed and scattered electric fields, respectively, on each of the various surfaces (or regions) in Figure 2.

The operator  $L_s$  refers to the BOT surface  $S_s$  and is given by

$$L_s(\vec{J}) = j\omega\mu \iint_{\text{BOT}} \vec{J} \phi \, ds - \frac{1}{j\omega\epsilon} \nabla_s \iint_{\text{BOT}} (\nabla_s \cdot \vec{J}) \phi \, ds , \quad (1a)$$

where the free-space Green's function is  $\phi = 1/4\pi R \exp(-jkR)$ ,  $\vec{J}$  denotes the current density on  $S_s$ ,  $R$  is the distance from the source to the field point,  $\nabla_s$  is the surface gradient on the BOT,  $\omega$  is the radian frequency (sinusoidal excitation is assumed), and  $\mu$  and  $\epsilon$  are the permeability and permittivity of the medium, respectively. For the caps, the operator  $L_c(\cdot)$  is identical to  $L_s(\cdot)$  except the domain of integration spans the caps. Similarly, the operator  $L_e(\cdot)$  is identical to  $L_s(\cdot)$  except the domain of integration spans the edge region on either the BOT or the caps. Analogously for the wire part,

$$L_w(\vec{J}) = j\omega\mu \int_{\text{wire}} \vec{J} \phi \, dh - \frac{1}{j\omega\epsilon} \vec{u}_w \frac{d}{dh} \int_{\text{wire}} \frac{d\vec{J}}{dh} \phi \, dh , \quad (1b)$$

where  $L_w(\vec{J})$  is the one-dimensional operator on the wire current density and  $\vec{u}_w$  is a unit vector along the wire. The operator in the junction region  $L_j(\cdot)$  is  $L_w(\vec{J})$ , where the domain of integration is restricted to the attachment segment  $S_a$ ;  $L_j(\cdot)$  is  $L_s(\cdot)$  when the surface integration is confined to the disk part of the junction region  $S_d$  (Figure 2).

To solve Equation (1) for the unknown current density  $\vec{J}$  on the entire BOT configuration, explicit expressions must be obtained for all operators. We use the Galerkin (MM) technique to expand the currents specific to each region where the curved BOT surface is subdivided into axial strips, the caps into

trapezoidal patches, the wire radiators into connected straight-wire segments, the junction region into an attachment and a disk part, and the edge region into patches on the BOT and the caps. A set of basis and testing functions for the unknown currents in each of these regions is introduced. The basis sets for the wires and the junctions are identical to those given in Reference 3.

#### 4.2 Basis Functions for the Currents

First, the expansion of the currents on the BOT surface is considered. The two orthogonal components of the surface currents on the BOT, i.e.,  $\vec{J}^{st}$  and  $\vec{J}^{sz}$ , are expanded in terms of a modal expansion along  $z$  and in overlapping triangle functions along the  $t$ -direction. Specifically, the currents on the  $i$ -th axial segment of the BOT are

$$\vec{J}_i^s = \sum_n (I_{ni}^{st} \vec{J}_{ni}^{st} + I_{ni}^{sz} \vec{J}_{ni}^{sz}) \quad (\text{amperes/meter}), \quad (2)$$

where

$$\vec{J}_{ni}^{s\alpha} = \vec{u}_\alpha f_i^\alpha(t) v_n^\alpha(z), \quad \alpha = t \text{ or } z \quad (2a)$$

and

$$v_n^\alpha(z) = \begin{cases} \exp(jn\pi z/L) & , \quad \alpha = t \\ \exp(jn\pi z/L) - (-1)^n & , \quad \alpha = z \end{cases} \quad (2b)$$

The modal expansion term  $v_n^\alpha(z)$  spans all integer  $n$  values from  $-N$  to  $+N$ .  $I_{ni}^{st}$  and  $I_{ni}^{sz}$  represent the orthogonal current components in the  $t$ - and  $z$ -directions, respectively, corresponding to the  $i$ -th surface triangle function  $f_i^\alpha(t)$ , where

$$f_j^\alpha(t) = \begin{cases} 1 - |t'|, & |t'| < 1 \\ 0, & |t'| > 1 \end{cases}, \quad t' = t - t_j. \quad (2c)$$

(The axial component of current  $\vec{J}_{ni}^{sz}$  is chosen to vanish at the ends of the BOT.)

On the caps, the currents are expanded in terms of two components along  $\vec{u}_t$  and  $\vec{u}_\rho$ , where  $\rho$  is a polar coordinate on the caps (Figure 3), yielding for the  $l$ -th trapezoidal patch

$$\vec{J}_l^c = \vec{u}_t I_l^{ct} J_l^{ct} + \vec{u}_\rho I_l^{cp} J_l^{cp}, \quad (3)$$

where

$$J_l^{c\alpha} = f_l^\alpha(t) g_l^\alpha(\rho), \quad \alpha = t \text{ or } \rho \quad (3a)$$

and  $f_l^\alpha(t)$  and  $g_l^\alpha(\rho)$  are triangle functions spanning the cap surfaces. (In general,  $\vec{u}_t \cdot \vec{u}_\rho \neq 0$ .) For maximum flexibility in surface representation, the patches are allowed to be nonuniform so that the triangle functions can vary from patch to patch. (For alternate patch representations, see References 29 and 30.)

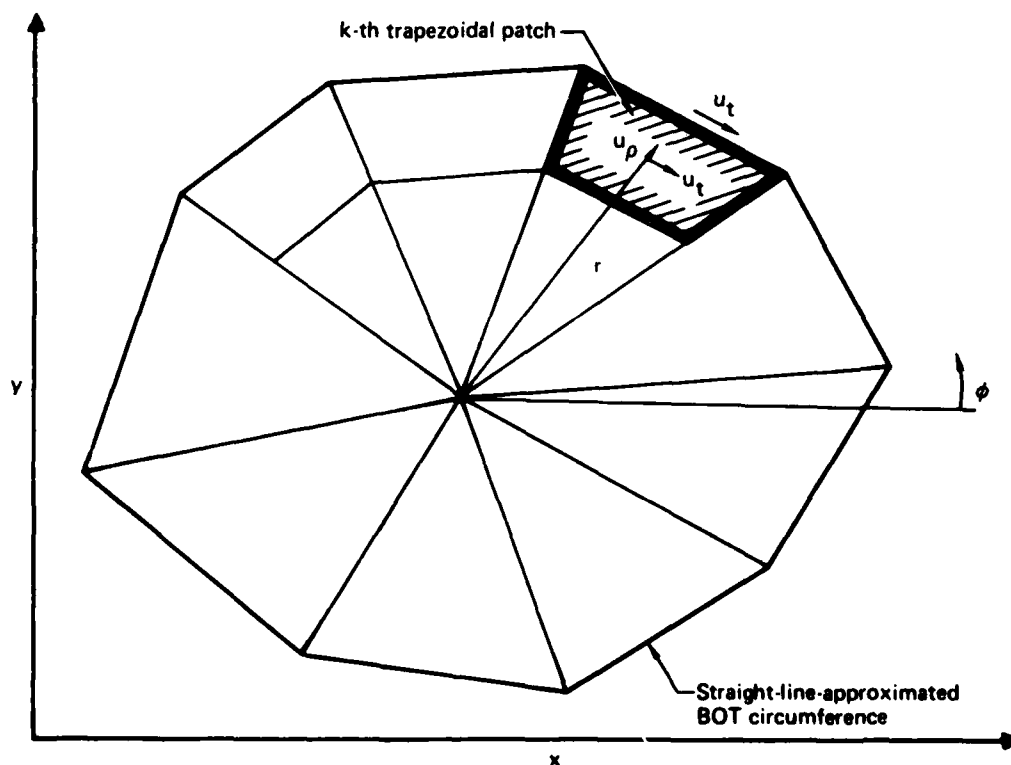


Figure 3. Detail of cap coordinate geometry.

The basis functions for the wire and the junction currents are those given in Reference 3, and for completeness, they are repeated here. On the  $l$ -th wire segment, the filamentary wire current can be expressed as

$$\vec{J}_l^w = \vec{u}_l^w I_l^w T_l(h) \quad (\text{amperes}), \quad (4)$$

where  $\vec{u}_l^w$  is a unit vector along the  $l$ -th segment,  $T_l(h)$  denotes a triangle function (Figure 2a), and  $I_l^w$  is the unknown wire-current coefficient associated with the  $l$ -th segment. For a wire segment nearest the attachment point, one-half of a wire triangle function overlaps the half-triangle basis term on the attachment segment. This representation yields a piece-wise continuous (p.c.) current from the junction to the wire.

The junction current  $\vec{J}^j$ , in terms of basis functions associated with the wire attachment segment  $S_a$  and the disk region  $S_d$ , is given as

$$\vec{J}^j(p) = I^j \begin{cases} \vec{J}_a^j, & p \in S_a \\ \vec{J}_d^j, & p \in S_d \end{cases} \quad (\text{amperes/meter}), \quad (5)$$

where

$$\vec{J}_a^j = \vec{u}_a \frac{T_a(h)}{2\pi a}, \quad (5a)$$

$$\vec{J}_d^j = -\vec{u}_r \frac{1}{2\pi r} \left( \frac{b-r}{b-a} \right), \quad (5b)$$

and  $\vec{u}_a$  and  $T_a(h)$  are an outward-directed unit vector and a half-triangle function on the attachment segment, respectively;  $\vec{u}_r$  is a unit vector on the (annular) disk surface away from the wire,  $r$  is the radial distance on the disk,  $b$  is the outer disk radius,  $a$  is the wire radius, and  $I^j$  is the unknown junction current coefficient.

The edge region spans the rims of the caps ( $S_c$ ) and the ends of the BOT surface ( $S_g$ ) (Figure 4). The edge currents are defined as

$$\vec{J}_l^e(p) = I^e \begin{cases} \vec{J}_l^{ce}, & p \in S_c \\ \vec{J}_l^{se}, & p \in S_g \end{cases} \quad (\text{amperes}), \quad (6)$$

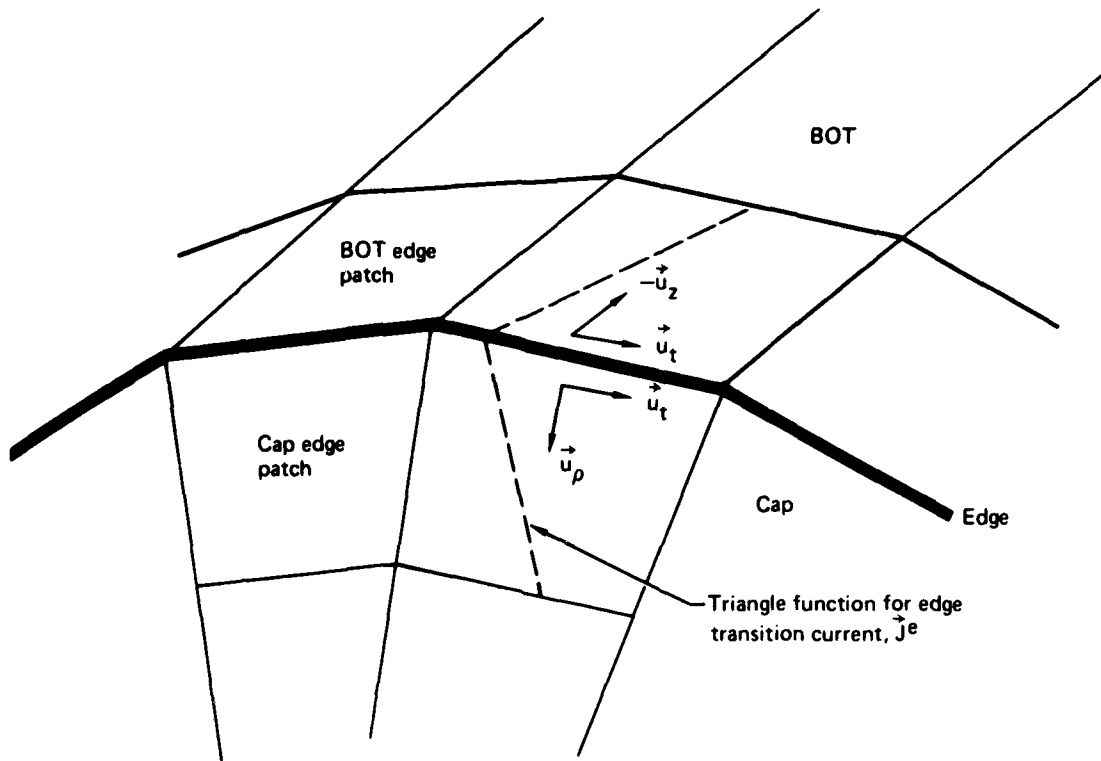


Figure 4. Detail of edge region.

where

$$\vec{J}_l^{ce} = \vec{u}_\rho f^\rho(t) h^\rho(\rho), \quad (6a)$$

$$\vec{J}_l^{se} = \pm \vec{u}_z f^z(t) h^z(z), \quad z = \mp L, \quad (6b)$$

and  $h^\rho(\rho)$  and  $h^z(z)$  denote half-triangle functions on the cap and BOT edge regions, respectively. (The t-components of the currents in the edge region are contained in the expansion set for  $\vec{J}^{ct}$  and  $\vec{J}^{st}$ .)

#### 4.3 Impedance Expressions

The expansions for the currents on the BOT surface, the caps, the wire segments, the junction, and the edge region, given in Equations (2)-(6), are substituted into Equation (1). The inner product of the integral operators  $L(\cdot)$  in Equation (1) is formed with the testing functions  $\vec{W} (= \vec{J}^*)$  via the

Galerkin technique. A system of linear equations for the unknown current coefficients,  $I_{ni}^{st}$ ,  $I_{ni}^{sz}$ ,  $I_l^{ct}$ ,  $I_l^{cp}$ ,  $I_l^w$ ,  $I_j$ , and  $I^e$  is obtained, written in matrix form as

$$\begin{bmatrix}
 Z_{-m,-m}^{ss} & & & & Z_{-m,m}^{ss} & & & \\
 & \ddots & & & & \ddots & & \\
 & & Z_{oo}^{ss} & & & & & \\
 & & & \ddots & & & & \\
 & & & & Z_{m,m}^{ss} & & & \\
 & & & & & Z_m^{sw} & Z_m^{sj} & Z_m^{sc} & Z_m^{se} \\
 & & & & & Z_n^{ws} & & & \\
 & & & & & & Z_n^{jw} & & \\
 & & & & & & & Z_n^{cw} & \\
 & & & & & & & & Z_n^{ew} & Z_n^{ej} & Z_n^{ec} & Z_n^{ee}
 \end{bmatrix}
 \begin{bmatrix}
 I^s \\
 I^w \\
 I^j \\
 I^c \\
 I^e
 \end{bmatrix}
 =
 \begin{bmatrix}
 V^s \\
 V^w \\
 V^j \\
 V^c \\
 V^e
 \end{bmatrix}
 \quad (7)$$

The right column vector in these equations represents a generalized voltage vector, and the  $Z$  elements are the familiar impedances defining the EM interactions between various parts of the body in Figure 2. For example, the BOT-surface interactions are given by  $Z_{mn}^{ss}$ . Similarly, the cap-cap, the BOT-cap, the wire-wire, the BOT-wire, BOT-junction, wire-junction, and the junction-junction interactions are defined by  $Z^{cc}$ ,  $Z_m^{sc}$ ,  $Z^{ww}$ ,  $Z_m^{sw}$ ,  $Z_m^{sj}$ ,  $Z^{wj}$ , and  $Z^{jj}$ , respectively. The remaining elements refer to the edge interactions.

The composition of the system matrix in Equation (7) is determined by the particular configuration under analysis. For example, if the radiating (or parasitic) wire element in Figure 2 is not attached to the BOT surface (i.e., as in the case of radiative coupling), the junction-related elements can be deleted from the system matrix, Equation (7). Similarly, if there are no off-surface (wire) antennas on the BOT, the system matrix contains only elements of  $Z_{mn}^{ss}$ ,  $Z^{cc}$ ,  $Z_m^{sc}$ , and the edge-related elements.

Specific analytical expressions for the various matrices in Equation (7) can be obtained by evaluating the inner products having the form



$$Z = \langle \vec{W}, L(\vec{J}) \rangle = \iint_S ds \iint_{S'} ds' jnk \left[ \vec{W} \cdot \vec{J} - \frac{1}{k^2} (\nabla \cdot \vec{W})(\nabla \cdot \vec{J}) \right] \phi, \quad (8)$$

where all superscripts and subscripts on  $\vec{W}$  and  $\vec{J}$  are omitted for simplicity and  $S$  and  $S'$  refer to surfaces containing the field and source points, respectively;  $\eta = \sqrt{\mu/\epsilon}$  and  $k = 2\pi/\lambda$ . (For the choice of basis functions used in this discussion, Equation (8) is an alternate expression to the one given in Equation (1a) and is easier to program.) Equation (8) is evaluated for each of the regions of Figure 2. Computer implementation forms for the impedance elements are derived in Appendix A.

#### 4.3.1 Junction-Independent Impedance Matrices

First, the matrices in Equation (7) independent of the junction will be considered. The derivation of the elements of these matrices is rather involved and will be relegated to Appendix A. Only the formal definitions and summary of results are given here.

The BOT interaction matrix  $Z_n^{ss}$  can be partitioned into submatrices corresponding to the  $t$  and  $z$  directed current components, i.e.,

$$Z_{mn}^{ss} = \begin{bmatrix} Z_{mn}^{ss,tt} & Z_{mn}^{ss,tz} \\ Z_{mn}^{ss,zt} & Z_{mn}^{ss,zz} \end{bmatrix}. \quad (9)$$

The  $(i,j)$ -th element of these submatrices is obtained from

$$Z_{mn,ij}^{ss,\alpha\beta} = \langle \vec{W}_{mi}^{s\alpha}, L_s(\vec{J}_{nj}^{s\beta}) \rangle, \quad (10)$$

where  $\alpha, \beta$  are combinations of  $t$  and  $z$ , and  $m$  and  $n$  are the mode numbers of the axial expansion (Equation (2b));  $\vec{W}_{mi}^{s\alpha}$  and  $\vec{J}_{nj}^{s\beta}$  are the  $i$ -th testing and the  $j$ -th current basis functions, respectively, on the BOT surface.

$Z_{mn}^{ss}$  is canonically similar to the system matrix arising from the MM analysis for BORS (Reference 5). However, in the present case, the set of expansion functions used is not orthonormal to  $L(\cdot)$  as in the BOR case, and thus there is no modal decoupling. Hence all  $Z_{mn}^{ss}$  matrices are present, not

just the diagonal ones. Using the expansion for  $\vec{J}^s$  in Equation (2) and noting that for any vector  $\vec{A}$  in the BOT coordinate system,

$$\nabla \cdot \vec{A} = \frac{\partial A_t}{\partial t} + \frac{\partial A_z}{\partial z}, \quad (11)$$

explicit expressions for the  $Z_{mn}^{ss}$  elements can be obtained from Equation (10). These matrix elements are summarized in Appendix A.1.

The cap interaction matrix  $Z^{cc}$  is partitioned into  $t$  and  $\rho$  (= polar coordinate) components depicted in Figure 3, i.e.,

$$Z^{cc} = \begin{bmatrix} Z^{cc,tt} & | & Z^{cc,t\rho} \\ \hline Z^{cc,\rho t} & | & Z^{cc,\rho\rho} \end{bmatrix} \quad (12)$$

with the  $(k, l)$ -th element defined as

$$Z_{kl}^{cc,\alpha\beta} = \langle \vec{W}_k^{c\alpha}, L_c(\vec{J}_l^{c\beta}) \rangle, \quad \alpha, \beta = t \text{ or } \rho \quad (13)$$

where  $\vec{W}_k^{c\alpha}$  and  $\vec{J}_l^{c\beta}$  are the  $k$ -th testing and  $l$ -th current basis functions on the corresponding patches, respectively. For maximum generality, the patches can be trapezoidal. For any vector  $\vec{A}$  in the cap-coordinate system,

$$\nabla \cdot \vec{A} = \frac{1}{\rho} \frac{\partial A^t}{\partial t} + \frac{\partial A_\rho}{\partial r} + \frac{A^\rho}{r}, \quad (14)$$

where  $r \equiv \bar{r}\rho$  with  $0 < \rho < 1$  and  $r$  is a sector ray, i.e., the distance from the origin on the cap to a sample point defining the generating curve of the BOT (Figure 3). The scaling factor  $\bar{r}$  may be different in each patch. Using Equations (3) and (14), the expressions for  $Z_{kl}^{cc,\alpha\beta}$  can be derived as shown in Appendix A.2.

The BOT-cap interaction matrix  $Z_m^{sc}$  is partitioned as

$$Z_m^{sc} = \begin{bmatrix} Z_m^{sc,tt} & | & Z_m^{sc,t\rho} \\ \hline Z_m^{sc,\rho t} & | & Z_m^{sc,\rho\rho} \end{bmatrix}, \quad (15)$$

where the  $t$  coordinate on the caps and on the BOT surface is the same. The  $(i, l)$ -th element of the matrix in Equation (15) is given by

$$Z_{m,il}^{sc,\alpha\beta} = \langle \tilde{w}_{mi}^{s\alpha}, L_c(\tilde{j}_l^{c\beta}) \rangle, \quad \alpha = t \text{ or } z; \beta = t \text{ or } \rho \quad (16)$$

where  $\tilde{w}_{mi}^{s\alpha}$  and  $\tilde{j}_l^{c\beta}$  are the  $i$ -th testing function on the BOT and the  $l$ -th current basis function on the cap, respectively. Explicit expressions for  $Z^{sc}$  are derived in Appendix A.3. The cap-BOT matrices are obtained from  $Z_{m,lj}^{cs,\alpha\beta} = Z_{-m,jl}^{sc,\alpha\beta}$ .

The  $(k, l)$ -th wire-wire interaction matrix elements are defined as

$$Z_{kl}^{ww} = \langle \tilde{w}_k^w, L(\tilde{j}_l^w) \rangle, \quad (17)$$

where  $\tilde{w}_k^w$  is the  $k$ -th wire testing function and  $\tilde{j}_l^w$  is the  $l$ -th wire current basis function. The explicit form for  $Z_{kl}^{ww}$ , given in Table 1, is computed using a program based on the approach in Reference 11.

The BOT-wire interaction matrix  $Z_m^{sw}$  is also partitioned into  $t$  and  $z$  components, i.e.,

$$Z_m^{sw} = \begin{bmatrix} Z_m^{sw,t} \\ Z_m^{sw,z} \end{bmatrix} \quad (18)$$

with the  $(i, l)$ -th element defined as

$$Z_{n,il}^{sw,\alpha} = \langle \tilde{w}_{ni}^{s\alpha}, L_w(\tilde{j}_l^w) \rangle, \quad \alpha = t \text{ or } z \quad (19)$$

where  $\tilde{w}_{ni}^{s\alpha}$  is the  $i$ -th BOT surface testing function and  $\tilde{j}_l^w$  is the  $l$ -th wire current basis function. The explicit forms for the  $Z_{n,il}^{sw,\alpha}$  matrix elements are derived in Appendix A.4. The wire-BOT interaction matrix elements are obtained from  $Z_{n,lj}^{ws,\alpha} = Z_{-n,jl}^{sw,\alpha}$ . An analogous development, described in Appendix A.5, yields the cap-wire interaction matrix elements,  $Z^{cw}$ .

TABLE 1. JUNCTION AND WIRE IMPEDANCE ELEMENTS.

<p>Junction-Junction element</p> $Z_{jj} = \frac{jk\eta}{4\pi} \int_0^{h_0} dh' \int_0^{h_0} dh \left\{ T_a(h') T_a(h) (\vec{u}_a' \cdot \vec{u}_a) - \frac{T_a'(h') T_a'(h)}{k^2} \right\} \frac{e^{-jkR}}{R}$ $+ \frac{jk\eta}{16\pi^3 (b-a)^2} \int_{-\pi}^{\pi} d\varphi' \int_a^b dr' \int_{-\pi}^{\pi} d\varphi \int_a^b dr \left\{ (b-r')(b-r) (\vec{u}_r' \cdot \vec{u}_r) - \frac{1}{k^2} \right\} \frac{e^{-jkR}}{R}$ $+ \frac{jk\eta}{8\pi^2 (b-a)} \int_0^{h_0} dh \int_a^b dr \int_{-\pi}^{\pi} d\varphi \left\{ T_a(h) (r-b) (\vec{u}_a \cdot \vec{u}_r) - \frac{T_a'(h)}{k^2} \right\} \frac{e^{-jkR}}{R}$ $+ \frac{jk\eta}{8\pi^2 (b-a)} \int_0^{h_0} dh \int_a^b dr \int_{-\pi}^{\pi} d\varphi \left\{ T_a(h) (r-b) (\vec{u}_a \cdot \vec{u}_r) - \frac{T_a'(h)}{k^2} \right\} \frac{e^{-jkR}}{R}$
<p>Wire-Junction matrix elements</p> $Z_{\ell j}^w = \frac{jk\eta}{4\pi} \int_{\ell} dh' \int_0^{h_0} dh \left\{ T(h') T_a(h) (\vec{u}_{\ell}^w \cdot \vec{u}_a) - \frac{T'(h) T_a'(h)}{k^2} \right\} \frac{e^{-jkR}}{R}$ $+ \frac{jk\eta}{8\pi^2 (b-a)} \int_{\ell} dh' \int_a^b dr \int_{-\pi}^{\pi} d\varphi \left\{ T(h') (r-b) (\vec{u}_{\ell}^w \cdot \vec{u}_r) - \frac{T'(h')}{k^2} \right\} \frac{e^{-jkR}}{R}$
<p>Wire-Wire matrix elements</p> $Z_{k\ell}^{ww} = \frac{jk\eta}{4\pi} \int_k dh \int_{\ell} dh' \left\{ T(h) T(h') (\vec{u}_k^w \cdot \vec{u}_{\ell}^w) - \frac{1}{k^2} T'(h') T'(h) \right\} \frac{e^{-jkR}}{R}$

#### 4.3.2 Junction-Dependent Impedance Matrices

The derivation of junction-dependent impedance matrices parallels the development in Reference 3 for junction effects on BOR surfaces. For completeness, a synopsis of this development together with its extension to BOT geometries is given below. The junction element  $Z_{jj}$  is considered first. Referring to Equation (5), the junction basis function consists of a disk term and a wire attachment term. The planar annular disk patch  $S_d$  approximates the BOT surface at the junction point (Figure 2c). This

assumption is satisfactory when the disk radius  $b$  is much less than the BOT radius of curvature  $R$  at the attachment point (i.e.,  $b \ll R$ ) and the disk diameter is small compared to a wavelength. In practice, the latter condition is always met since the disk diameter is taken to be the width of a BOT surface triangle function (i.e., usually  $< 0.1\lambda$  in width). Analytical predictions using this approach correlate well with measured data, confirming the efficacy of the planar disk approximation. Explicitly,  $Z^{jj}$  can be written as

$$Z^{jj} = \langle \vec{w}_a^j, L_j(\vec{j}_a^j) \rangle + \langle \vec{w}_d^j, L_j(\vec{j}_d^j) \rangle + \langle \vec{w}_d^j, L_j(\vec{j}_a^j) \rangle + \langle \vec{w}_a^j, L_j(\vec{j}_d^j) \rangle. \quad (20)$$

The resulting four terms describe the wire (attachment) segment, the disk, the disk-wire, and the wire-disk interactions. The inner products in Equation (20) are evaluated using Equation (8) and the fact that

$$\nabla \cdot \vec{j} = \begin{cases} \frac{1}{2\pi a} T'_a(h) & \text{if } \vec{j} = \vec{j}_a^j \\ \frac{1}{r} \frac{d}{dr} (rJ^r) & \text{if } \vec{j} = \vec{j}_d^j \end{cases} \quad (21)$$

and similarly for  $\nabla \cdot \vec{w}$ . The divergence for  $\vec{j} = \vec{j}_d^j$  is expressed in terms of the coordinate system of the planar disk and implies that in the disk region, the radial component of current  $J^r$  is much greater than the azimuthal component. In evaluating the integrals in Equation (8), those integrals corresponding to the wire attachment segment reduce to one-dimension. Explicit forms for all terms of  $Z^{jj}$  in Equation (2) are summarized in Table 1.

The wire-junction matrix elements are defined as

$$Z_\ell^{wj} = \langle \vec{w}_\ell^w, L_j(\vec{j}_a^j) \rangle + \langle \vec{w}_\ell^w, L_j(\vec{j}_d^j) \rangle, \quad (22)$$

where  $\vec{w}_\ell^w$  is the  $\ell$ -th wire testing function. The expressions for  $Z_\ell^{wj}$  are given in Table 1. The junction-wire matrix  $Z^{jw}$  is the transpose of  $Z^{wj}$ .

The BOT-junction impedance elements are given by

$$Z_{m,i}^{sj,a} = \langle \vec{w}_{mi}^{sa}, L_j(\vec{j}_a^j) \rangle + \langle \vec{w}_{mi}^{sa}, L_j(\vec{j}_d^j) \rangle, \quad (23)$$

where  $\alpha = t$  or  $z$ ,  $m$  is the mode number, and  $\tilde{w}_{mi}^{sa}$  is the testing function associated with the  $i$ -th BOT axial strip. Explicit forms for the terms in Equation (23) are obtained in Appendix A.6. The junction-BOT matrix elements are obtained from  $Z_{n,i}^{js,\alpha} = Z_{-n,i}^{sj,\alpha}$ .

#### 4.3.3 Edge-Dependent Impedance Matrices

The edge transition region is subdivided into a region on the BOT and cap surfaces, respectively. (This procedure is analogous to treatment of the junction region.) We consider first the interaction between the  $k$ -th and  $l$ -th edge regions, which in terms of the respective testing and current expansion functions is given as

$$\begin{aligned} Z_{kl}^{ee} = & \langle \tilde{w}_k^{ce}, L_e(\tilde{j}_l^{ce}) \rangle + \langle \tilde{w}_k^{se}, L_e(\tilde{j}_l^{se}) \rangle \\ & + \langle \tilde{w}_k^{se}, L_e(\tilde{j}_l^{ce}) \rangle + \langle \tilde{w}_k^{ce}, L_e(\tilde{j}_l^{se}) \rangle. \end{aligned} \quad (24)$$

The first term on the right side of Equation (24) is identical to the expression for  $Z_{kl}^{ccpp}$  (Equation (A.16d)), except the triangle functions are replaced by half triangle functions denoted as  $h$  functions. The remaining terms of Equation (24) are evaluated in Appendix A.7.

The interaction of the BOT surface with the edge region is formally given by

$$Z_{m,il}^{se,\alpha} = \langle \tilde{w}_{mi}^{sa}, L_e(\tilde{j}_l^{ce}) \rangle + \langle \tilde{w}_{mi}^{sa}, L_e(\tilde{j}_l^{se}) \rangle, \quad (\alpha = t \text{ or } z) \quad (25)$$

where the first term on the right side is identical to  $Z_{m,il}^{sc,\alpha p}$  where the triangle functions over the primed variables are replaced by half-triangle functions, i.e., the  $g$  functions in Equations (A-20c) and (A-20d) become  $h$  functions. The explicit expression for the second term is developed in Appendix A.7.

Similarly, the interaction of the caps with the edge region is expressed as

$$Z_{kl}^{ce,\alpha} = \langle \tilde{w}_k^{ca}, L_e(\tilde{j}_l^{ce}) \rangle + \langle \tilde{w}_k^{ca}, L_e(\tilde{j}_l^{se}) \rangle, \quad (\alpha = t \text{ or } p). \quad (26)$$

The first term above on the right side is identical to  $Z_{kl}^{cc,\alpha q}$  when the  $g$  functions subscripted by  $q$  in Equations (A-16c) and A-16d) are replaced by half triangles. The second term is derived in Appendix A.7. All edge interaction matrices retain the usual symmetry so that, for example, the edge-BOT interactions are given by

$$Z_{m,li}^{es,\alpha} = Z_{-m,il}^{se,\alpha}$$

and the edge-cap interactions are the transpose of  $Z_{kl}^{ce,\alpha}$ .

Finally, the wire radiator-edge interactions are defined as

$$Z_{ij}^{we} = \langle \tilde{w}_i^w, L_e(J_j^{ce}) \rangle + \langle \tilde{w}_i^w, L_e(J_j^{se}) \rangle, \quad (27)$$

where the first term on the right side is identical to  $Z_{ij}^{wc,\rho}$ , where  $f_j$  is replaced with half triangles  $h_j$ . The second term is given in Appendix A.7. The edge-wire interactions are transposes of Equation (27).

#### 4.4 General Structure and Properties of the $Z_{BOT}$ Matrix

The  $Z_{BOT}$  matrix in Equation (7) is composed of partitioned submatrices  $Z_{mn}^{ss,\alpha\beta}$  (Equation (9)) corresponding to the orthonormal vectors spanning the BOT surface. The overall structure is shown in Figure 5. In general, this matrix is full since there is no modal decoupling. (In the MM/BOR analysis, only the matrices  $Z_{mm}$  along the principal diagonal are present.) However, certain symmetries exist for  $G_{mn}$  and  $Z_{mn}^{ss}$  that reduce the fill time of the  $Z_{BOT}$  matrix. Specifically,

$$\begin{aligned} G_{mn} &= {}_t(G_{mn}) \\ Z_{mn}^{sstt} &= {}_t(Z_{mn}^{sstt}) \\ {}_m{}_t(Z_{mn}^{sstz}) &= -{}_n(Z_{mn}^{sszt}) \\ Z_{mn}^{sszz} &= {}_t(Z_{mn}^{sszz}), \end{aligned} \quad (28)$$

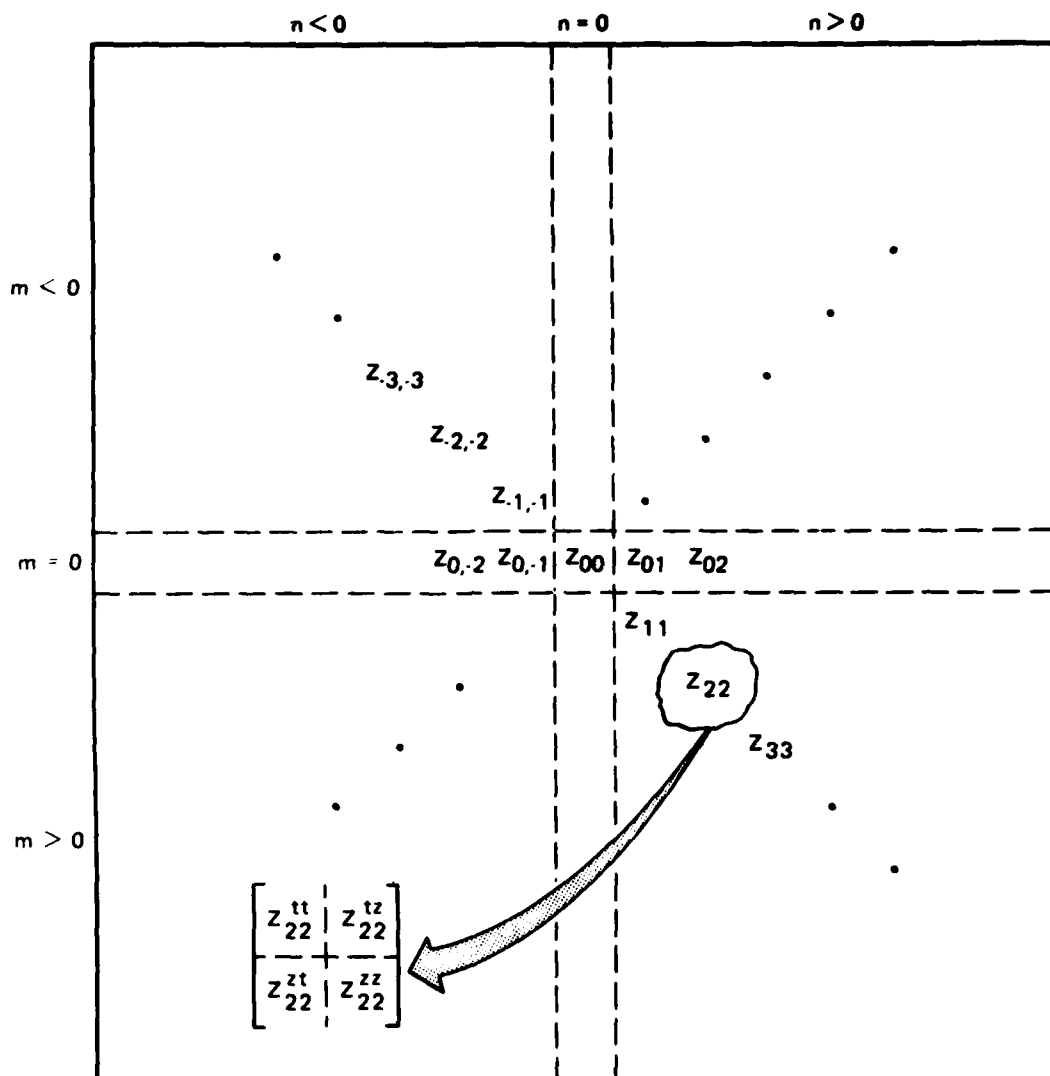


Figure 5. Structure of  $Z_{BOT}$  matrix.

where  ${}_t(G_{mn})$  denotes the transpose of  $G_{mn}$ . In the implementation of the analysis, only the lower triangular quadrant of the  $Z_{BOT}$  matrix is computed, i.e., the partitioned submatrices are filled for  $0 < m < NMODE$ , and  $-m < n < m$ , where  $NMODE$  is the total number of axial modes (including  $m = 0$ ) used in this analysis. The matrix fill times for each impedance element in MM/BOR and MM/BOT are about the same. Furthermore, detailed examination of the  $G_{mn}(i,j)$  function shows that it is maximum when  $m = n$  and  $i = j$ , i.e., the largest values occur on the main diagonal of the  $Z_{BOT}$  matrix, and the self-



terms contribute the most. These properties lead to a diagonally strong overall matrix. To compute the inverse of  $Z_{BOT}$ , the entire  $Z_{BOT}$  matrix must be filled, which can be accomplished from the following symmetry relations:

$$\begin{aligned}
 Z_{n,m}^{sstt} &= Z_{m,n}^{sstt} & \frac{(-m, -n)}{Z_{m,n}^{sstt}} &= Z_{m,n}^{sstt} & \frac{(-n, -m)}{Z_{m,n}^{sstt}} &= Z_{m,n}^{sstt} \\
 Z_{n,m}^{sszt} &= -t(Z_{m,n}^{sstz}) & &= -Z_{m,n}^{sszt} & &= -t(Z_{m,n}^{sszt}) \\
 Z_{n,m}^{sstz} &= -t(Z_{m,n}^{sszt}) & &= -Z_{m,n}^{sstz} & &= -t(Z_{m,n}^{sstz}) \\
 Z_{n,m}^{sszz} &= Z_{m,n}^{sszz} & &= Z_{m,n}^{sszz} & &= Z_{m,n}^{sszz}
 \end{aligned} \tag{29}$$

These relations are exploited in the computer algorithm to minimize the fill-time and aid in solution of the matrix equations arising in the formulation. If the BOT surface has several (physical) planes of symmetry, additional relations can be established within each of the partitioned submatrices, permitting further computational savings. In summary, the  $Z_{BOT}$  matrix is composed of diagonally strong matrices, possessing certain symmetries and dominantly intercoupled only for neighboring modes.

## 5. FAR-FIELD RADIATION AND SCATTERING ANALYSIS

Having obtained expressions for all elements in the overall system matrix (Equation (7)), the unknown current vector  $I$  is determined when the applied excitation (voltage vector) is specified. (In a scattering analysis, the incident field is specified.) Formally the radiated field in  $\beta$  ( $= \theta$  or  $\phi$ ) polarization, found from the currents  $I$  on the entire configuration, is<sup>5</sup>

$$\vec{E}_r^\beta = \frac{-j\omega\mu}{4\pi r} e^{-jkr} [\tilde{R}^\beta] [I], \quad (30)$$

where the row transfer matrix  $\tilde{R}^\beta$  consists of contributions from the BOT, the caps, the wire (radiators), the junction, and the edge regions. As an example, the  $i$ -th transfer matrix for the BOT is defined as

$$(\tilde{R}_n^{s,\alpha\beta})_i = \langle \vec{J}_{ni}^{s\alpha}, \vec{E}_r^\beta \rangle, \quad (31)$$

where the superscript  $\alpha$  denotes  $t$  or  $z$ , and  $\beta$  denotes the  $\theta$  or  $\phi$  polarization of the radiated field  $\vec{E}_r^\beta$ , given in spherical coordinates as,

$$\vec{E}_r^\beta = \vec{u}_\beta^r e^{jk(\rho \sin \theta_r \cos \phi_r + z \cos \theta_r)}, \quad (32)$$

where the field point of measurement is at  $\theta_r, \phi_r$ , and  $\rho$  is the distance to a point on the BOT surface, measured from the origin (see Figure 6). Expressing the inner product in Equation (31) explicitly, the transfer matrices are given as

$$(\tilde{R}_n^{s,\alpha\beta})_i = \int_1 dt \int_{-L}^L dz (\vec{u}_\alpha^r \cdot \vec{u}_\beta^r) f_i^\alpha(t) v_n^\alpha(z) e^{jk\psi}, \quad (33)$$

where  $\psi = \rho \sin \theta_r \cos \phi_r + z \cos \theta_r$ . Referring to Figure 6, the unit vectors in Equation (33) for the BOT geometry are given by

$$\vec{u}_t = \vec{u}_x \cos \nu + \vec{u}_y \sin \nu, \quad \vec{u}_z$$

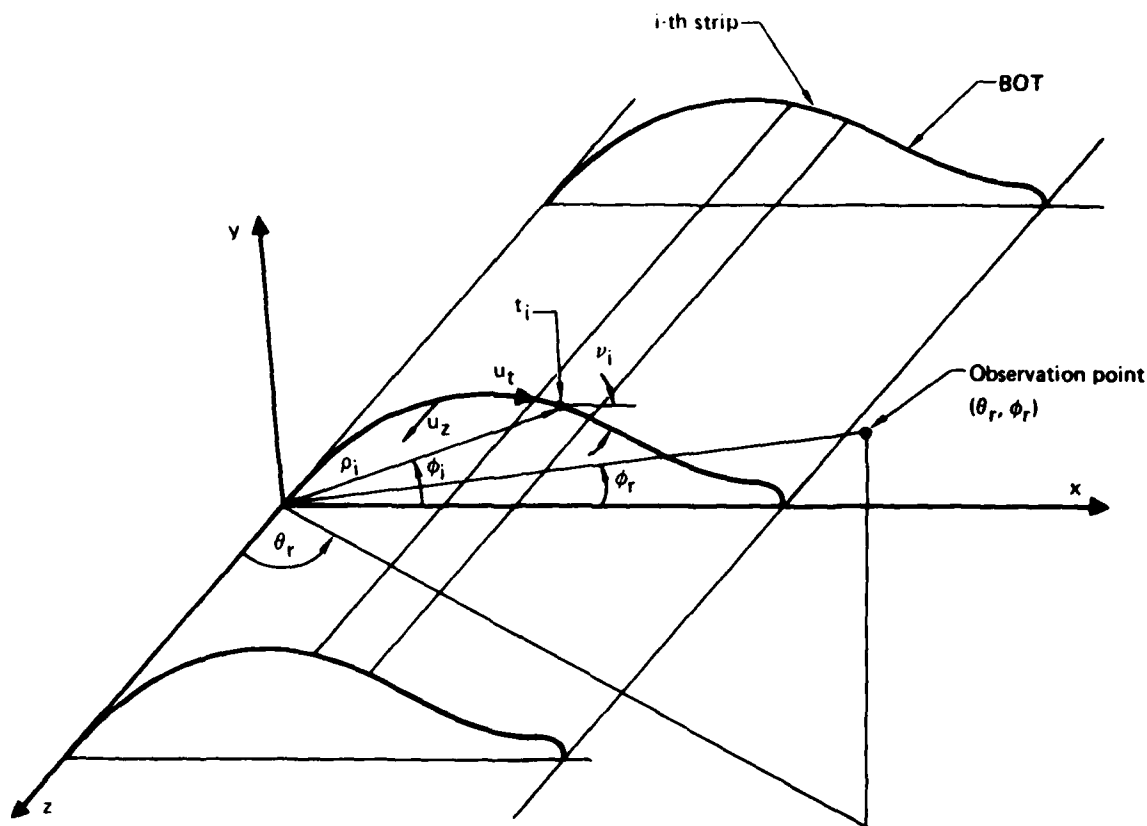


Figure 6. Coordinate geometry for transfer matrix evaluation on the BOT.

and

$$\vec{u}_{\theta}^r = \vec{u}_x \cos \theta_r \cos \phi_r + \vec{u}_y \cos \theta_r \sin \phi_r - \vec{u}_z \sin \theta_r$$

$$\vec{u}_{\phi}^r = -\vec{u}_x \sin \phi_r + \vec{u}_y \cos \phi_r.$$

Using a centroid approximation for the  $t$ -integration, a pulse approximation for the triangle functions  $f_1^a(\cdot)$ , and Equation (2b), explicit expressions for the transfer matrices are obtained as summarized in Table 2. Analogously, the transfer matrices for the cap, wire, junction, and edge regions, i.e.,  $R^C$ ,  $R^W$ ,  $R^J$ , and  $R^e$ , summarized in Table 2 can be obtained. Using these  $R$ -matrices, the far-field power radiation patterns and the scattering cross sections can be computed.

TABLE 2 TRANSFER MATRIX ELEMENTS

BOT Transfer Matrix Elements

$$R_{ni}^{s,t\theta} = \cos \theta_r D_n^t \sum_{p=1}^4 \Delta t_p T_p^t \cos(\nu_p - \phi_r) A_p^r$$

$$R_{ni}^{s,z\theta} = -\sin \theta_r D_n^z \sum_{p=1}^4 \Delta t_p T_p^z A_p^r$$

$$R_{ni}^{s,t\phi} = D_n^t \sum_{p=1}^4 \Delta t_p T_p^t \sin(\nu_p - \phi_r) A_p^r$$

$$R_{n,i}^{s,z\phi} = 0$$

where

$$A_p^r = e^{jk(x_p \cos \phi_r + y_p \sin \phi_r) \sin \theta_r}$$

$$D_n^t = 2L \operatorname{sinc}(\xi)$$

$$D_n^z = 2L \{ \operatorname{sinc}(\xi) - (-1)^n \operatorname{sinc}(K \cos \theta_r) \}$$

$$\xi = n\pi + K \cos \theta_r, K = kL$$

Cap Transfer Matrix Elements

$$R_k^{c,t\theta} = \cos \theta_r \sum_{p=1}^{16} A_p \cos(\nu_p - \phi_r) f_p^t g_p^t A_p^r$$

TABLE 2 TRANSFER MATRIX ELEMENTS (Continued)

$$R_k^{c,\rho\theta} = \cos \theta_r \sum_{p=1}^{16} A_p \cos(\phi_p - \phi_r) f_p^\rho g_p^\rho A_p^r$$

$$R_k^{c,t\phi} = \sum_{p=1}^{16} A_p \sin(\phi_p - \phi_r) f_p^t g_p^t A_p^r$$

$$R_k^{c,\rho\phi} = \sum_{p=1}^{16} A_p \sin(\phi_p - \phi_r) f_p^\rho g_p^\rho A_p^r$$

where

$$A_p^r = e^{jk(x_p \cos \phi_r + y_p \sin \phi_r) \sin \theta_r + z_p \cos \theta_r}$$

#### Wire Transfer Matrix Elements

$$R_\ell^{w,\theta} = \sum_{p=1}^4 \{(\Delta x_p \cos \phi_r + \Delta y_p \sin \phi_r) \cos \theta_r - \Delta z_p \sin \theta_r\} T_p A_p^r$$

$$R_\ell^{w,\phi} = \sum_{p=1}^4 (-\Delta x_p \sin \phi_r + \Delta y_p \cos \phi_r) T_p A_p^r$$

where  $A_p^r$  is evaluated on p-th wire segment

#### Junction Transfer Matrix Elements

$$R^j, \theta = R_a^{w,\theta} - \left(\frac{b-a}{8}\right) \sum_{q=1}^4 \{\sin \alpha_q \cos \theta_r \cos(\phi_d - \phi_r) - \cos \alpha_q \sin \theta_r\} A_q^r$$

TABLE 2 TRANSFER MATRIX ELEMENTS (Concluded)

$$R^{j,\phi} = R_a^{w,\phi} + \left( \frac{b-a}{8} \right) \sum_{q=1}^4 \sin \alpha_q \sin(v_d - \phi_r) A_q^r$$

where  $A_q^r$  is evaluated on the junction disk and  $R_a^{w,\alpha}$  = transfer matrix for attachment segment identical to  $R^{w,\alpha}$  with  $T_p \rightarrow h_p$ .

Edge Transfer Matrix Elements

$$R_1^{e,\beta} = \sum_{p=1}^8 \left\{ A_p f_p^t(t) h_p^t(\rho) \bar{A}_p^r + \Delta s_p f_p^t(t) h_p^t(z) A_p^r \right\} (\vec{u}_t \cdot \vec{u}_\beta^r)$$

where

$$\vec{u}_t \cdot \vec{u}_\theta^r = \cos \theta_r \sin(v_p - \phi_r)$$

$$\vec{u}_t \cdot \vec{u}_\phi^r = \sin(v_p - \phi_r)$$

$A_p$  = trapezoidal edge patch on cap

$\Delta s_p$  = edge patch on BOT

and  $\bar{A}_p^r$  is evaluated at the center of  $A_p$  on the cap;  $A_p^r$  is evaluated at the center of  $\Delta s_p$  on the BOT.

In general the far-field power gain in  $\beta$ -polarization is given by

$$g_{\beta} = \frac{k^2 \eta}{4\pi P_0} |\tilde{R}^{\beta} I|^2, \quad (34)$$

where

$$P_0 = \text{Re}\{\tilde{V} Z^{-1} V^*\} \quad (34a)$$

and

$$I = Z^{-1} V. \quad (34b)$$

The current vector  $I$  is obtained by solving the system of linear equations [Equation (7)], subject to a specified voltage excitation  $V$  determined by the location and electrical characteristics of embedded or off-surface wire antennas on the body, considered in more detail below.

### 5.1 Embedded Antennas

We consider first the case of embedded (slot) antennas on capped BOT surfaces. The gain is calculated from Equation (34), where

$$\tilde{R}^{\beta} = [\tilde{R}_n^{s,\beta} \mid \tilde{R}^{c,\beta}] \text{ and } V = \begin{bmatrix} v_n^s \\ v^c \end{bmatrix}.$$

The elements of the  $R$  matrices are given in Table 2;  $I$  is computed using a system matrix  $Z$  containing only the impedances of the BOT, caps, edges, and their respective interactions. It is assumed that there are no antennas on the caps; hence  $v^c = 0$ . The form of the excitation voltage vector  $v_n^s$  depends

upon the type and location of the antenna on the BOT. As an example, consider a series of K aperture (slot) antennas embedded in the BOT surface and centered at  $(t_k, z_k)$ ,  $k = 1, 2, \dots, K$ . Assuming that the apertures are rectangular, then if the aperture at the  $i$ -th axial strip subtends one triangle function  $f_i(t)$  and an axial width of  $(z_1 - z_0)$ ,

$$v_{ni}^{s\alpha} = \langle \vec{w}_{ni}^{s\alpha}, \vec{E}_i \rangle$$

$$= \int_1 dt f_i(t) \int_{z_0}^{z_1} dz \vec{u}_\alpha \cdot \vec{E}_i(t, z) v_n^\alpha(z), \alpha = t \text{ or } z \quad (35)$$

where  $v_n^\alpha(z)$  is the BOT basis function in Equation (2b). In general, the aperture excitation function  $\vec{E}_i(t, z)$  can be specified to be of any form. For this discussion, let the slot be uniformly excited by  $E_i$  (V/m) in the  $\alpha$ -polarization, so that

$$\vec{E}_i^\alpha = \vec{u}_\alpha E_i \begin{cases} 1, & |z| \leq |z_1 - z_0| \\ 0, & \text{otherwise} \end{cases} \quad (36)$$

Then

$$v_{ni}^\alpha = a_{ni}^\alpha U_i^\alpha, \quad (37)$$

where

$$U_i^\alpha = \int_1 f_i(t) dt \quad (38)$$

and

$$a_{ni}^\alpha = \begin{cases} (z_1 - z_0) E_i, & n = 0 \\ \frac{L}{jn\pi} \left( e^{jn\pi \frac{z_1}{L}} - e^{jn\pi \frac{z_0}{L}} \right) E_i, & n \neq 0 \end{cases} \quad (39)$$



In the above expressions, it is assumed that the  $i$ -th slot is excited uniformly in the  $t$  and/or  $z$  polarization by an electric field,  $E_i$ , which may be a complex quantity. In the program, if  $V_{ni}^a \neq 0$ , then  $(U^a)_i$  is represented by an array of the form

$$U = \begin{bmatrix} 0 \\ \vdots \\ U_i^t \\ \vdots \\ 0 \\ \vdots \\ 0 \\ \vdots \\ U_i^z \\ \vdots \\ 0 \end{bmatrix} \quad (40)$$

If the slots are excited solely in the  $t$ -polarization,  $U_i^z = 0$ . For simplicity,  $U_i^t$  and  $U_i^z$  can be set equal to unity. By obvious extension, these results can be generalized for a BOT containing a series of slots at a given axial strip, as in the case of two-dimensional antenna arrays.

If the BOT is uncapped (i.e., an open surface), the expression in Equation (34) can be written more explicitly as

$$g_\beta = \frac{k_n^2}{4\pi P_o} \left| \sum_{m,n} \tilde{R}_m^{s\beta} Y_{mn}^{ss} V_n^s \right|^2, \quad (41)$$

where

$$P_o = \sum_{m,n} \text{Re} \{ \tilde{V}_m^s Y_{mn}^{ss} V_n^{s*} \}. \quad (42)$$

The matrix  $Y_{mn}^{ss}$  denotes the partitioned submatrix corresponding to the (m,n)-th modes in the inverted  $Z_{BOT}$  matrix. The expression for the  $V_n^s$  matrices remains unchanged.

## 5.2 Off-Surface Radiators

In this case, the gain is computed from Equation (34) where

$$\tilde{R}^{\beta} = [\tilde{R}_n^{s,\beta} | \tilde{R}^{c,\beta} | \tilde{R}^{w,\beta} | \tilde{R}^{j,\beta} | \tilde{R}^{e,\beta}]$$

and

$$V = \begin{bmatrix} V_n^s \\ V^c \\ V^w \\ V^j \\ V^e \end{bmatrix}.$$

If we excite the closed BOT with both off-surface wire radiators and aperture antennas,  $V_n^s$  and  $V^w$  must be specified. For the latter, the nonzero element of the column vector corresponds to the segment of the wire that is actively fed. For an attached wire antenna,  $V^j$  also is specified. For a parasitic radiator, on the other hand,  $V^j = 0$ . Examples using this formulation for wire radiators are given in Section 7. In all cases in the present discussion, we assume that  $V^c$  and  $V^e$  are null column vectors, i.e., no active radiators are on the caps and edge regions.

## 5.3 Scattering Fields

In general, the scattering cross section in terms of the transfer matrices in Table 2 is given as

$$\frac{\sigma^{pq}}{\lambda^2} (\theta_i, \phi_i, \theta_s, \phi_s) = \frac{k^2 \eta^2}{4\pi\lambda^2} \left| \tilde{R}^p Z^{-1} R^q \right|^2, \quad (43)$$

where  $q$  and  $p$  denote the polarization of the incident and scattered fields;  $(\theta_i, \phi_i)$  and  $(\theta_s, \phi_s)$  are the incident and scattering angles, and the transfer matrices  $R_m^\beta$  ( $\beta = p, q$ ) express the relations between the current on the BOT, cap, edge regions, and an observation point in free space. Examples of cross sections for a closed cylinder, represented as a BOT computed using this expression are given in Section 7. In general, the present formulation also can treat general BOT configurations with attached wire scatterers, as was done for BOR-wire geometries in Reference 17.

## 6. NEAR-FIELD AND ANTENNA COUPLING ANALYSIS

In the preceding sections, the radiated and scattered fields were computed at field points sufficiently distant from the bodies that the respective fields were planar and their components transverse. Using the previously computed currents on the body, the near-fields (electric and magnetic) at points  $< \lambda$  distant from the radiating or scattering surfaces can be computed. Generally, all six field components must be determined to specify the near-fields. In the subsequent sections, the present formulation is specialized first for the electric near-fields, followed by the corresponding results for the magnetic fields. Last, antenna coupling problems will be addressed.

### 6.1 Electric Near-Field Formulation

In general, the electric field at a free-space point  $r$ , resulting from a surface current density  $\vec{J}$  on the surface of a body in Figure 2, is given by

$$\vec{E}(r) = L_s(\vec{J}^s) + L_c(\vec{J}^c) + L_w(\vec{J}^w), \quad (44)$$

where  $L(\cdot)$  denotes the integral operators, defined earlier in Equations (1a) and (1b), over the currents on the BOT, cap, and wire segments of the configuration in Figure 2. The contribution from the junction and edge regions is assumed negligible and is deleted.

In this discussion, the current is induced on the body by an incident wave (as in a scattering problem) or by an active aperture or antenna attached to, or radiatively coupled to, the BOT surface. It is convenient to reexpress the operator  $L_s(\vec{J}^s)$  in Equation (1a) for this analysis as

$$L_s(\vec{J}^s) = j\omega\mu \iint_S \left[ \vec{J}^s \phi + \frac{1}{\omega^2 \mu \epsilon} (\nabla \cdot \vec{J}^s) (\vec{r} - \vec{r}') \phi_1 \right] ds' \quad (45)$$

using the relation

$$\nabla \iint_S (\nabla' \cdot \vec{J}) \phi(\vec{r} - \vec{r}') ds' = \iint_S (\nabla' \cdot \vec{J}) (\vec{r} - \vec{r}') \phi_1(\vec{r} - \vec{r}') ds',$$

where  $\phi_1(\vec{r} - \vec{r}') = [(1/R^2) + j(k/R)]\phi(\vec{r} - \vec{r}')$  and  $\phi(\vec{r} - \vec{r}')$  is the free-space Green's function. The operator for  $L_c(\vec{J}^c)$  is identical to Equation (45), except  $S$  spans the trapezoidal patches on the caps. Similarly,  $L_w(\vec{J}^w)$  is the one-dimensional analog of Equation (45).

First, the near-field contributions from the currents on the BOT surface alone will be computed. Substituting the expansion for  $\vec{J}^s$  (Equation (2)) into Equation (45) yields

$$\begin{aligned} \vec{E}_s(\vec{r}) = jk\eta \sum_{n,j} \iint_S ds' & \left\{ \left[ \vec{u}_t I_{nj}^{st} J_{nj}^{st} + \vec{u}_z I_{nj}^{sz} J_{nj}^{sz} \right] \phi(\vec{r}' - \vec{r}) \right. \\ & \left. + \frac{1}{k^2} \left[ I_{nj}^{st} \frac{\partial J_{nj}^{st}}{\partial t} + I_{nj}^{sz} \frac{\partial J_{nj}^{sz}}{\partial z} \right] (\vec{r}' - \vec{r}) \phi_1(\vec{r}' - \vec{r}) \right\}, \end{aligned} \quad (46)$$

where

$$\iint_S ds' = \int_{-L}^L dz' \int_j dt'.$$

Using the pulse approximations for the triangle expansion functions, Equation 46 can be written explicitly as

$$\begin{aligned} \vec{E}_s(\vec{r}) \approx jk\eta & \left\{ \vec{u}_x \sum_{n,j} \left[ I_{nj}^{st} \sum_{p=1}^4 \Delta t_p \left( T_p^t G_p^t \cos \nu_p + \frac{1}{k^2} (x_p - x) \dot{T}_p^t \bar{G}_p^t \right) \right. \right. \\ & \left. \left. + \frac{jn\pi}{k^2 L} I_{nj}^{sz} \sum_{p=1}^4 \Delta t_p (x_p - x) T_p^z \bar{G}_p^t \right] \right\} \end{aligned}$$

$$\begin{aligned}
& + \vec{u}_y \sum_{n,j} \left[ I_{nj}^{st} \sum_{p=1}^4 \Delta t_p \left( T_p^t G_p^t \sin v_p + \frac{1}{k^2} (y_p - y) \dot{T}_p^t \bar{G}_p^t \right) \right. \\
& + \left. \frac{jn\pi}{k^2 L} I_{nj}^{sz} \sum_{p=1}^4 \Delta t_p (y_p - y) T_p^z \bar{G}_p^t \right] \\
& + \vec{u}_z \sum_{n,j} \left[ I_{nj}^{st} \sum_{p=1}^4 \Delta t_p \left( \frac{1}{k^2} \right) \dot{T}_p^t H_p^t \right. \\
& + \left. I_{nj}^{sz} \sum_{p=1}^4 \Delta t_p \left( T_p^z G_p^z + \frac{jn\pi}{k^2 L} T_p^z H_p^t \right) \right] \Bigg\}, \quad (47)
\end{aligned}$$

where

$$G_p^\alpha = \int_{-L}^L dz' v_n^\alpha(z') \phi(\vec{r}_p - \vec{r}), \quad \alpha = t \text{ or } z \quad (47a)$$

$$H_p^\alpha = \int_{-L}^L dz' v_n^\alpha(z') (z_p - z) \phi_1(\vec{r}_p - \vec{r}), \quad (47b)$$

and  $\bar{G}_p^\alpha$  is obtained by replacing  $\phi$  with  $\phi_1$  in Equation (47a). The G and H functions are evaluated by numerical (Simpson) integration or by using a Taylor expansion for the integrals.

An analogous expression is obtained for the near-fields resulting from the currents on the caps. Replacing  $\vec{J}^s$  with  $\vec{J}^c$  and using the expansion in Equation (3) yields

$$\vec{E}_c(r) = jk\eta \sum_l \iint_{S_l} ds' \left\{ \left[ \vec{u}_t I_l^{ct} f_l^{ct} g_l^{ct} + \vec{u}_\rho I_l^{cp} f_l^{cp} g_l^{cp} \right] \Phi(\vec{r}_p - \vec{r}) + \frac{1}{k^2} \left[ I_l^{ct} f_l^{ct} g_l^{ct} \rho_l^{-1} + I_l^{cp} f_l^{cp} \hat{g}_l^{cp} \right] (\vec{r}_p - \vec{r}) \Phi_1(\vec{r}_p - \vec{r}) \right\}, \quad (48)$$

where  $\hat{g}_l^{cp} = (\vec{r}_l)^{-1} g_l^{cp} + r_l^{-1} g_l^{cp}$  and  $S_l$  is the  $l$ -th trapezoidal patch on the caps. The surface integral is evaluated using a four-pulse approximation for the triangle functions  $f$  and  $g$ . Thus for the  $l$ -th patch,

$$\iint_{S_l} ds' = \sum_{p=1}^{16} A_p,$$

where  $A_p$  is the area intercepted by the pulses. The total field attributable to the caps is obtained by summing the contributions over all patches. The resulting field can be decomposed into cartesian components if desired.

The near-field contribution of wire radiators (active and/or passive) on or near the BOT can be obtained by using the expansions for the wire currents:

$$\vec{E}_w(r) = jk\eta \sum_l \int_{\text{segment}} d\ell \left\{ \vec{u}_\ell J_\ell^w \Phi(\vec{r}_\ell - \vec{r}) + \frac{1}{k^2} \frac{\partial J_\ell^w}{\partial \ell} (\vec{r}_\ell - \vec{r}) \Phi_1 \right\}. \quad (49)$$

Using a centroid approximation for the integrals and a four-pulse representation for  $J_\ell^w$ ,

$$\begin{aligned} \vec{E}_w(r) = jk\eta \sum_l I_l^w \left\{ \vec{u}_x \sum_{p=1}^4 \Delta x_p T_p \Phi(\vec{r}_p - \vec{r}) + \frac{1}{k^2} \sum_{p=1}^4 \Delta \ell_p (x_p - x) \dot{T}_p \Phi_1(\vec{r}_p - \vec{r}) + \vec{u}_y [\dots] + \vec{u}_z [\dots] \right\}, \end{aligned} \quad (50)$$

where  $(x, x_p)$  are replaced by  $(y, y_p)$  and  $(z, z_p)$  in the  $\vec{u}_y$  and  $\vec{u}_z$  components, respectively. If the wires are attached to the BOT, the near-fields include the junction coupling effects since  $I_l^w$  is computed with the entire system matrix, including junction effects. (The direct contribution of the junction to the near-fields is negligible and was deleted in Equation (44).)

## 6.2 Magnetic Near-Field Formulation

In general, the magnetic field is given in terms of the vector potential  $\vec{A}$  and the incident field  $\vec{H}^i(r)$  as

$$\vec{H}(r) = \vec{H}^i(r) + \nabla \times \vec{A}(r), \quad (51)$$

where  $r$  is an arbitrary test point where the field is to be sampled. Letting  $\vec{H}^i(r) = 0$ , since there is no field at  $r$  except that caused by currents induced on the scattering or radiating surface  $S$ , Equation (51) becomes

$$\begin{aligned} \vec{H}(r) &= \nabla \times \iint_S \vec{J}(r) \Phi(\vec{r}' - \vec{r}) \, ds' \\ &= - \iint_S \vec{J}(r) \times (\vec{r}' - \vec{r}) \Phi_1(\vec{r}' - \vec{r}) \, ds', \end{aligned} \quad (52)$$

where  $\vec{J}$  encompasses the contributions from the BOT, the cap, and the wire surfaces. Again the direct contributions from the junction are omitted.

The near-field contribution from the BOT currents alone is computed first. Noting that the surface current density on the BOT can be decomposed into  $t$  and  $z$  components, Equation (52) can be written explicitly as



$$\begin{aligned}
\vec{H}_s(r) = & - \iint_S \left\{ \vec{u}_x \left[ (z' - z) \sin \nu' J_t - (y' - y) J_z \right] \right. \\
& + \vec{u}_y \left[ (x' - x) J_z - (z' - z) \cos \nu' J_t \right] + \vec{u}_z \left[ (y' - y) \cos \nu' J_t \right. \\
& \left. \left. - (x' - x) \sin \nu' J_t \right] \right\} \phi_1 ds' .
\end{aligned} \tag{53}$$

Using the modal expansion of the current components [Equation (2)] and evaluating the surface integrals in the same manner as in the electric near-field analysis, yields the following expression for  $\vec{H}_s(r)$ :

$$\begin{aligned}
\vec{H}_s(r) = & - \vec{u}_x \left\{ \sum_{n,j} \left[ I_{nj}^{st} \sum_{p=1}^4 \Delta t_p \sin \nu_p T_p^t H_p^t \right. \right. \\
& \left. \left. - I_{nj}^{sz} \sum_{p=1}^4 \Delta t_p (y_p - y) T_p^z \bar{G}_p^z \right] - \vec{u}_y \sum_{n,j} [\dots] \right. \\
& \left. + \vec{u}_z \sum_{n,j} \left[ I_{nj}^{st} \sum_{p=1}^4 \Delta t_p \left( (y_p - y) \cos \nu_p - (x_p - x) \sin \nu_p \right) T_p^t \bar{G}_p^t \right] \right\} ,
\end{aligned} \tag{54}$$

where the y-component is identical to the x-component, with the substitutions  $\sin \rightarrow \cos$  and  $(y_p - y) \rightarrow (x_p - x)$ . The G and H functions are defined in Equations (47a) and (47b).

Similarly, the contribution to the near-fields from the cap and wire currents are

$$\begin{aligned}
\vec{H}_c(r) \approx & - \left\{ \vec{u}_x \sum_{\ell} \left[ I_{\ell}^{ct} \sum_{p=1}^{16} A_p (z_p - z) \sin v_p f_p^{ct} g_p^{ct} \phi_{lp} \right. \right. \\
& + I_{\ell}^{cp} \sum_{p=1}^{16} A_p (z_p - z) \sin \phi_p f_p^{cp} g_p^{cp} \phi_{lp} \left. \right] \\
& - \vec{u}_y \sum_{\ell} [\cdot \cdot \cdot] \\
& + \vec{u}_z \sum_{\ell} \left[ I_{\ell}^{ct} \sum_{p=1}^{16} A_p \left( (y_p - y) \cos v_p - (x_p - x) \sin v_p \right) f_p^{ct} g_p^{ct} \phi_{lp} \right. \\
& + I_{\ell}^{cp} \sum_{p=1}^{16} A_p \left( (y_p - y) \cos \phi_p - (x_p - x) \sin \phi_p \right) f_p^{cp} g_p^{cp} \phi_{lp} \left. \right] \left. \right\} . \quad (55)
\end{aligned}$$

where the y-component is identical to the x-component, with  $\sin \rightarrow \cos$  and  $\phi_{lp} = \phi_l(\vec{r}_p - \vec{r})$ . Finally,

$$\begin{aligned}
\vec{H}_w(r) \approx & - \sum_{\ell} I_{\ell}^w \left\{ \vec{u}_x \sum_{p=1}^4 \left( (z_p - z) \Delta y_p - (y_p - y) \Delta z_p \right) T_p \phi_{lp} \right. \\
& + \vec{u}_y [\cdot \cdot \cdot] + \vec{u}_z [\cdot \cdot \cdot] \left. \right\} , \quad (56)
\end{aligned}$$

where in the y-component,  $(z_p - z) \Delta y_p + (x_p - x) \Delta z_p$  and  $(y_p - y) \Delta z_p + (z_p - z) \Delta x_p$ ; in the z-component, the corresponding terms are changed to  $(y_p - y) \Delta x_p$  and  $(x_p - x) \Delta y_p$ , respectively.

In the foregoing discussion, the electric and magnetic near-fields were sampled at a point. An alternate approach also was considered in which the fields were sampled and averaged over a rectangular patch. This latter

formulation was a generalization of that given in Reference 31. The predictions from the patch and point near-field analyses were compared for a number of BOT configurations. Numerical simulation showed that in regions where the electromagnetic wave departs significantly from being planar (i.e., in the vicinity of apertures), the point-sampled fields were more accurate, and thus this formulation was implemented here.

### 6.3 Coupling Analysis

The concept of coupling between adjacent antennas can be expressed in terms of the modal expansions and the admittance (or impedance) elements of the radiating body. The definitions and results obtained are a generalization of the lumped circuit concepts developed in Reference 36 (Chapters 13 and 14). In general, the mutual coupling, defined on a current basis (admittance) between ports  $i$  and  $j$  for a multi-port network, is

$$M_{ij} = \frac{\text{current at base of antenna (port) } i}{\text{open circuit voltage at antenna (port) } j} = \frac{I_i}{V_j} \quad (57)$$

when all other antennas are shorted (i.e.,  $V_k = 0$ , all  $k \neq j$ ). This definition is specialized below for coupling between wire and aperture antennas.

Case 1. Wire Antennas on a BOT - The coupling between wire antennas on a BOT is given in terms of the junction admittance matrix elements of the respective wire radiators. Hence if, for example, a BOT has two monopole wire radiators, the coupling between the two feed points is given by  $Y_{21}^{jj}$ , i.e., the junction admittance between junctions 2 and 1. Reciprocity requires that  $Y_{12}^{jj} = Y_{21}^{jj}$ . The coupling between other wire radiators, such as loops, can be obtained in similar fashion.

Case 2. Aperture Antennas on a BOT - In this case, we must consider spatially averaged coupling coefficients. An example will illustrate the point. Consider two slot antennas (t-polarized), each subtending single triangle functions. Let the slots be centered at  $(t_A, z_A)$  and  $(t_B, z_B)$  and have an axial half-length of  $L_A$  and  $L_B$ , respectively. Equation (57) can be written as

$$\langle M_{BA}^{tt} \rangle = \frac{\langle I_B^t \rangle}{\langle V_A^t \rangle}, \quad (58)$$

where the spatially averaged currents over the aperture area  $S_B$  are

$$\langle I_B^t \rangle = \iint_{S_B} \sum_{m,n} (Y_{BA}^{tt})_{mn} f(t_B) e^{jm\pi z/L} ds, \quad (58a)$$

and similarly,

$$\langle V_A^t \rangle = \iint_{S_A} \sum_m V_m^t f(t_A) e^{jm\pi z/L} ds. \quad (58b)$$

Carrying out the integrations over  $z$ ,

$$\langle I_B^t \rangle = \left\{ \sum_{m,n} (Y_{BA}^{tt})_{mn} \operatorname{sinc} \left( \frac{m\pi L_B}{L} \right) \exp(jm\pi L_{B/L}) \int_{t_B} f(t_B) dt \right\} \quad (59a)$$

and

$$\langle V_A^t \rangle = \left\{ \sum_m V_m^t \operatorname{sinc} \left( \frac{m\pi L_A}{L} \right) \exp(jm\pi L_{A/L}) \int_{t_A} f(t_A) dt \right\}. \quad (59b)$$

In the foregoing expressions,  $(Y_{BA}^{tt})_{mn}$  is the element of the admittance matrix [inverse of the system matrix in Equation (7)], corresponding to the axial BOT strips at  $t_A$  and  $t_B$ , and the  $m$  and  $n$  modes. By analogous considerations, a similar expression can be obtained for  $\langle M_{BA}^{zz} \rangle$ , associated with  $z$ -polarized slots.

## 7. VALIDATION AND APPLICATION OF THE GENERALIZED MM/BOT FORMULATION

The generalized MM/BOT formulation was used to predict the far fields radiated by embedded and off-surface wire antennas on various BOT configurations. In this study, both active and passive wire radiators were considered on open and closed (capped) BOTs, and the near-fields were computed in the vicinity of such antennas. Finally, the coupling between antennas was considered. The results from the analysis were compared with available published data supplemented with independent MDRL experimental measurements. Because of the proven reliability and accuracy of the MM/BOR codes developed by Mautz and Harrington at Syracuse University,<sup>5</sup> a significant part of the validation effort consisted of comparing results of the MM/BOR and MM/BOT formulations.

In subsequent examples, the far-field gain calculations are given in arbitrary units. When these calculations are compared with experimental data, the latter are used as the normalization. The results for the scattering cross sections and the near fields are given in absolute, unnormalized units.

### 7.1 Validation of the Far-Field Analysis

#### 7.1.1 Embedded (Slot) Antennas

Because of the availability of validated MM/BOR codes that treat apertures in surfaces of revolution,<sup>5,33</sup> the far-field radiation patterns were computed first for antennas located on BOR geometries, such as capped and open cylinders, modeled as a special case of a BOT. As an example, Figure 7 depicts a slot antenna of  $2.06\lambda$  length, subtending an angle of  $45^\circ$  and located on a cylinder with a radius and length of  $0.216\lambda$  and  $2.76\lambda$ , respectively. To facilitate comparison of the MM/BOT and MM/BOR results, the z-axis slot is  $\phi$ -polarized. The results from the two formulations, depicted in Figure 8, show excellent agreement. For the MM/BOR calculations, seven circumferential modes were used; for the MM/BOT analysis, four axial modes were employed. The pitch (vertical) and roll plane power radiation patterns are plotted in linear power, normalized to the MM/BOR results.

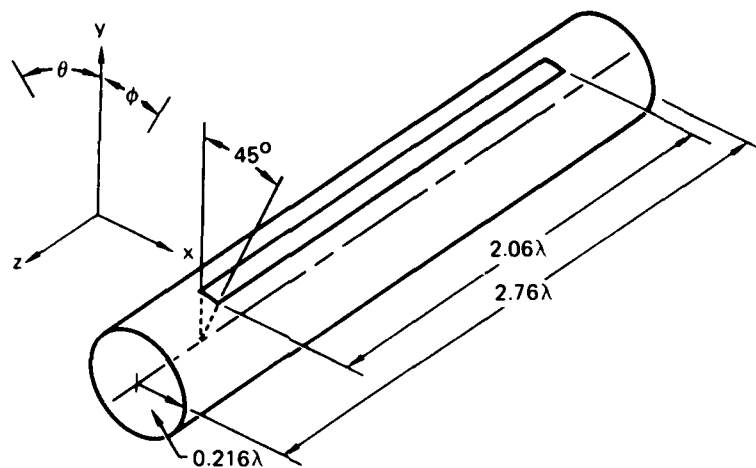


Figure 7. Slotted cylinder geometry.

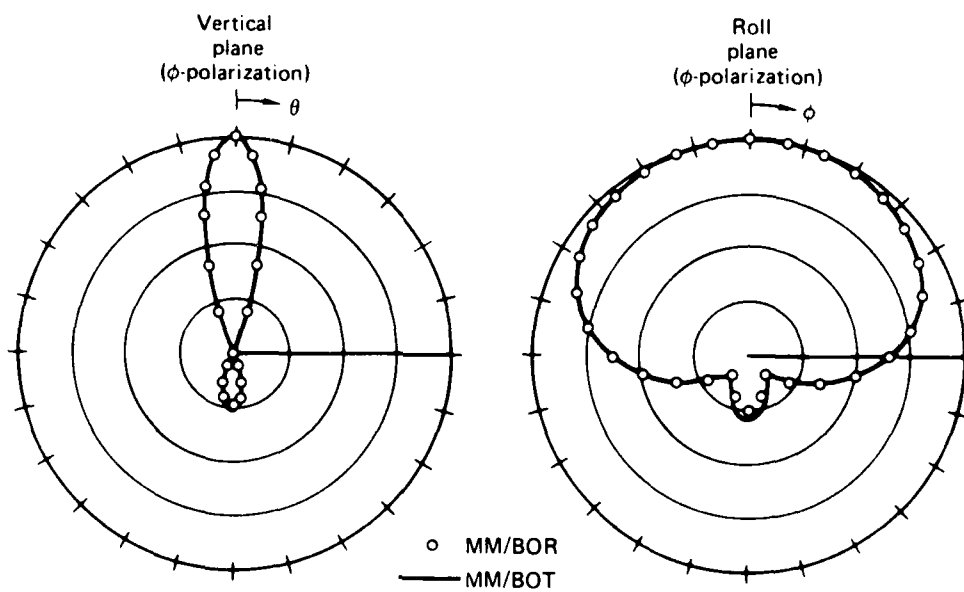


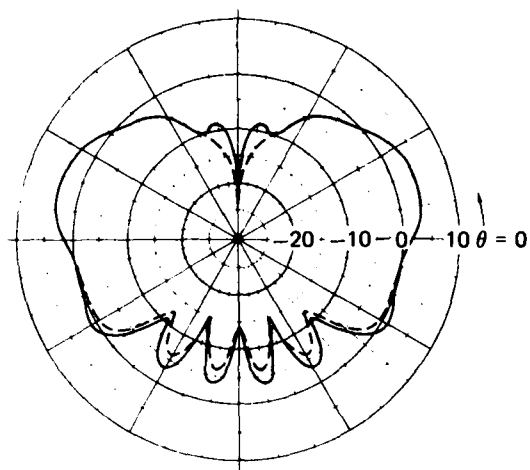
Figure 8. Comparison of MM/BOR and MM/BOT computed power radiation patterns: slotted cylinder ( $\phi$ -polarized slot).

### 7.1.2 Off-Surface Antennas

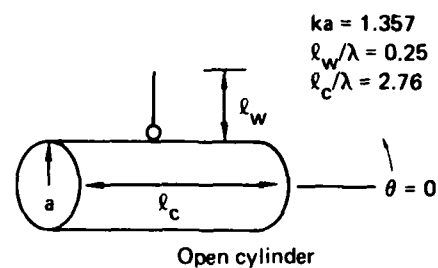
The treatment of off-surface antennas was examined extensively for monopoles on cylindrical structures. Initially, the simplest case was studied, namely monopoles on open cylinders. The validation baseline was the predictions using the MDRL-developed MM/BOR-wire analysis and experimental data.<sup>3</sup> The pitch and yaw plane patterns in  $\theta$  and  $\phi$  polarization are shown in Figure 9 for a quarter-wave monopole mounted at the mid-point of an open cylinder having  $ka = 1.357$  and a length of  $2.76\lambda$ . The MM/BOT results shown in Figure 9 are normalized to the MM/BOR-wire results. Results from the two analytical techniques are in close agreement. In Figure 10 the corresponding results are depicted for an active and a passive (parasitic) monopole located on the same cylinder. Again there is excellent agreement in the shape and location of the major pattern lobes and nulls.

Next, a capped cylinder of length  $\ell_c = 1\lambda$  and  $ka = 0.46$  with two attached quarter-wave elements was considered (Figure 11). The element at the cylinder mid-point was a base-fed monopole; the other attached element was unfed (passive). The MM/BOT predictions, compared with the results in Reference 3, are summarized in Figure 11. The radiation patterns were computed with and without the effect of the junction (current) interaction at the base of the unfed element. The predicted and measured results in Figure 11 clearly indicate the importance of including the junction interactions. In this case, the unfed stub acts as a reflecting element dramatically altering the directivity of the fed element. (The result without the junction interactions models a nonattached, radiatively coupled element, and the pattern can be obtained using the analysis in References 11 and 33.) The patterns are plotted in power using a linear (not decibel) scale and normalized to unity. Nine circumferential modes were used in the MM/BOR-wire analysis and four axial modes for the MM/BOT results.

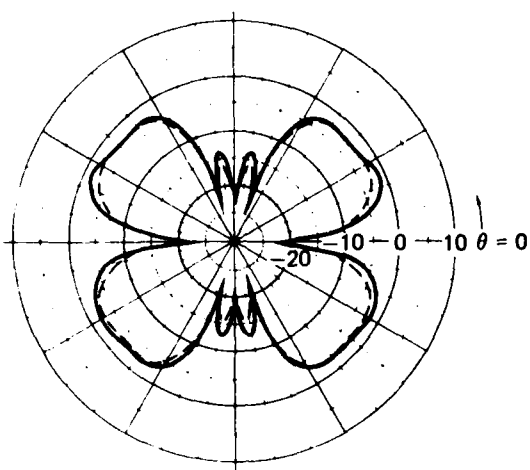
An application of the present formulation to wing-mounted antennas is depicted in Figure 12a where the yaw plane patterns for a monopole mounted on the trailing edge of a wing section are depicted. The section is  $2.76\lambda$  long. The wing coordinates are given in Sample Problem 3, Vol. II of this report. In Figure 12b the effect of an asymmetric active element on the radiation pattern is shown. Junctions were used at the antenna attachment points.



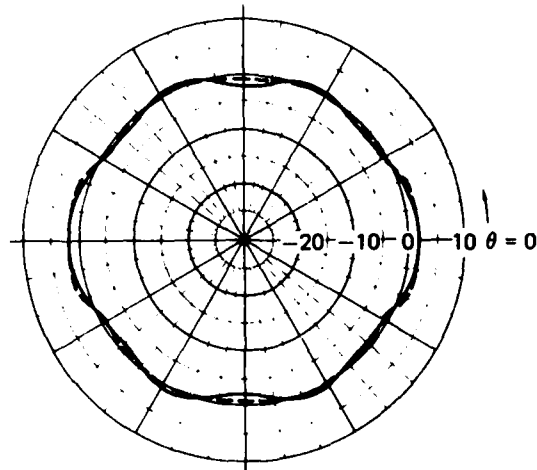
$\theta$  - polarization  
Pitch plane (dB)



— MM/BOT  
 --- MM/BOR



$\theta$  - polarization  
Yaw plane (dB)



$\phi$  - polarization  
Yaw plane (dB)

Figure 9. Comparison of MM/BOR and MM/BOT computed power radiation patterns: cylinder-mounted monopole.



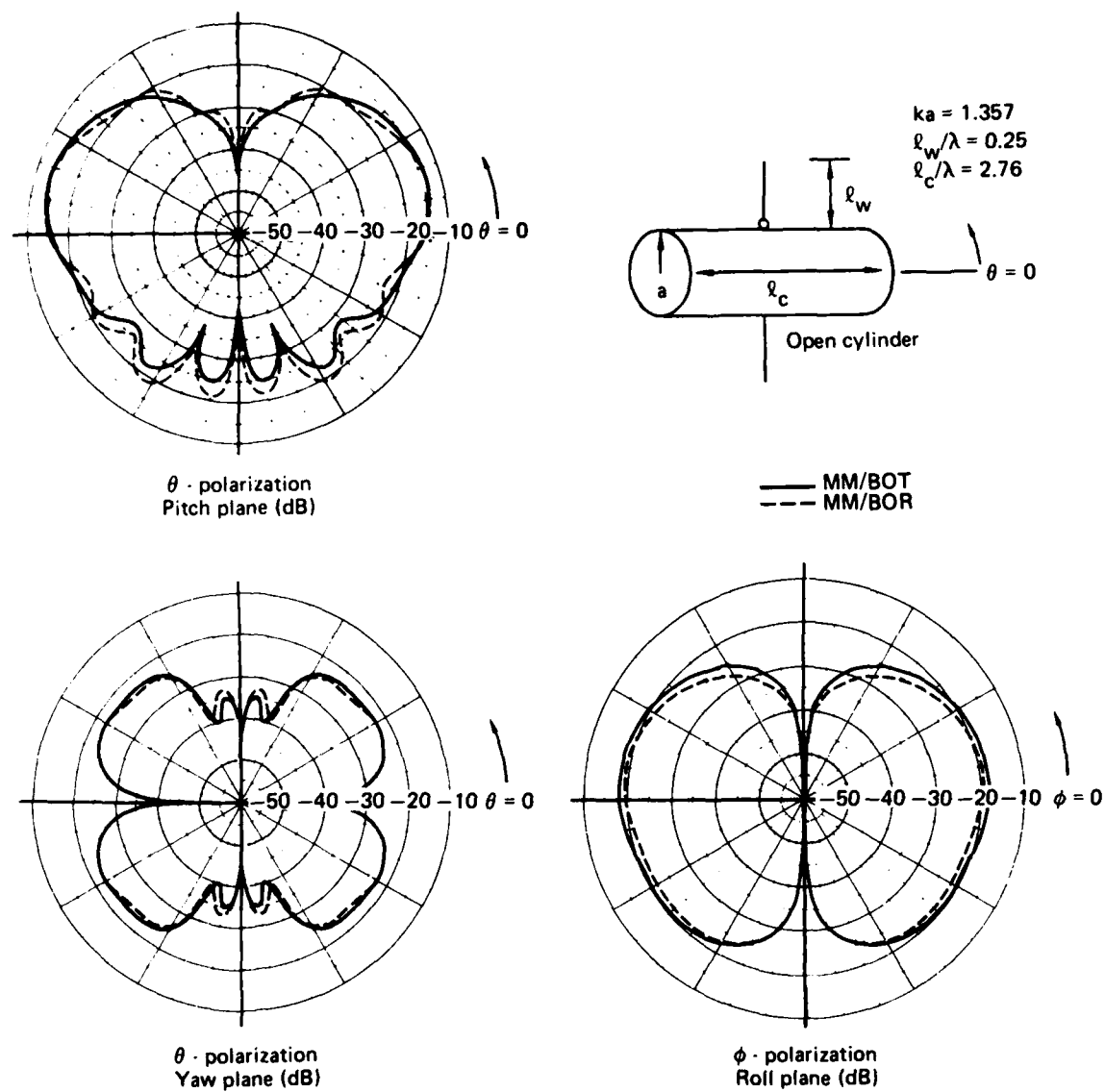


Figure 10. Comparison of MM/BOR and MM/BOT computed power radiation patterns: cylinder-mounted opposing monopoles (active and passive).

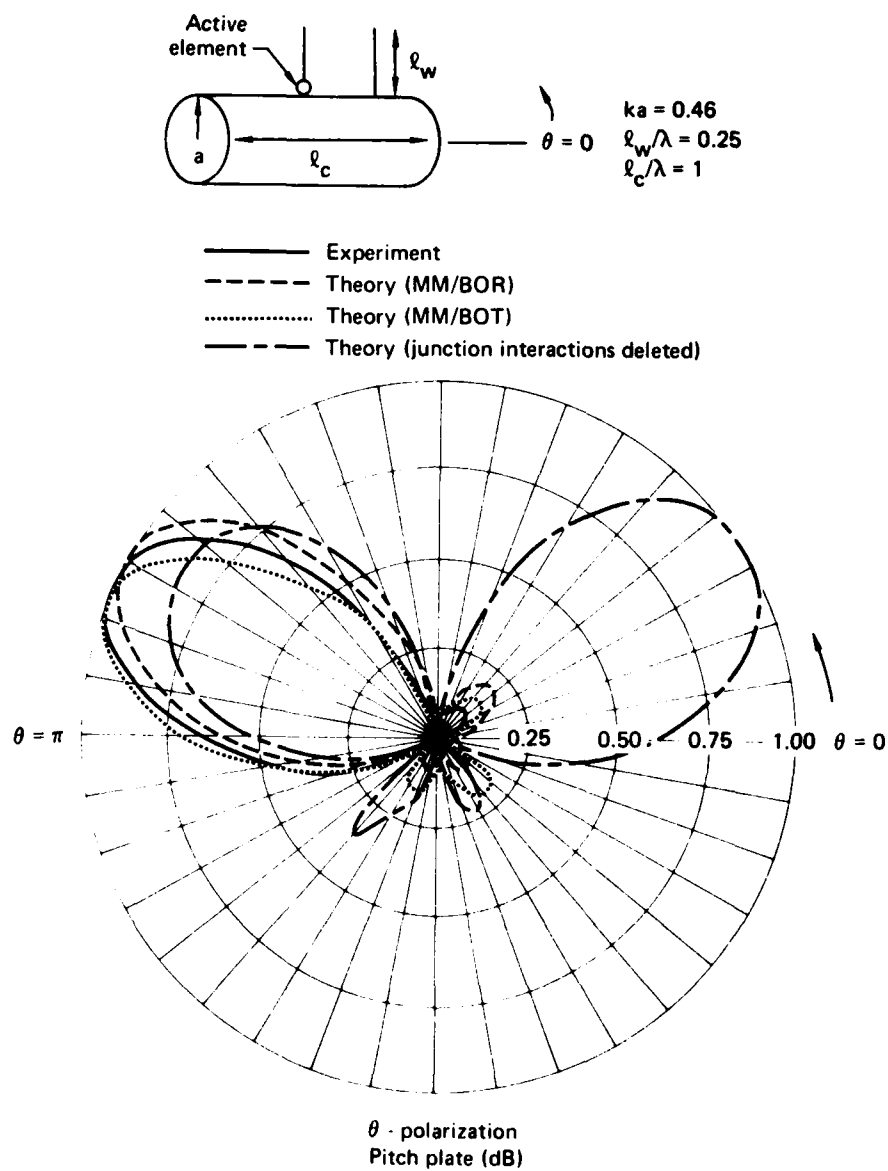
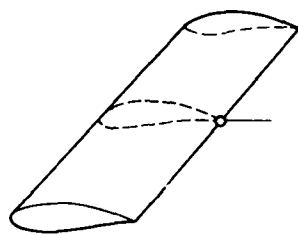
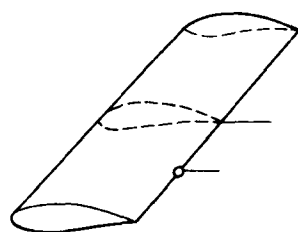


Figure 11. Comparison of MM/BOR and MM/BOT computed power radiation patterns with experiment: cylinder-mounted active and passive monopoles.



$1/8 \lambda$  monopole at mid-plane

$\theta$  - polarization  
 Frequency = 96.15 MHz  
 Yaw plane (dB)



$1/8 \lambda$  monopole at mid-plane element is parasitic

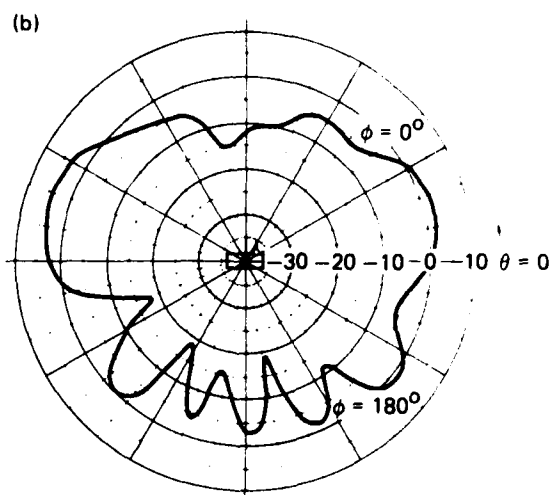
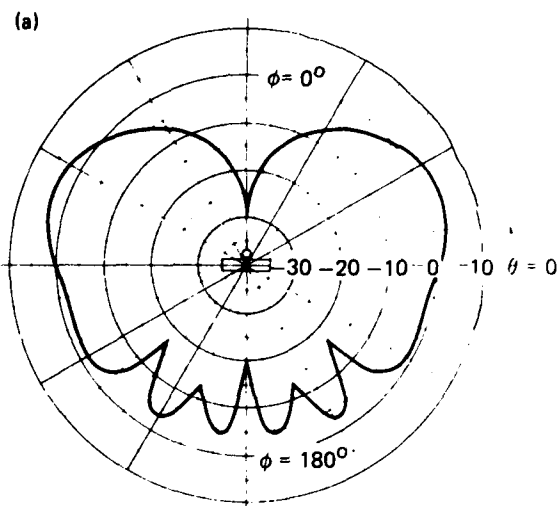


Figure 12. Power radiation patterns for wing-mounted monopoles.

## 7.2 Validation of the Scattering Analysis

Examples validating the scattering analysis in Section 5.3 are considered below. In Figure 13 the bistatic scattering cross section for an open cylinder of radius  $0.216\lambda$  and length  $2.76\lambda$  is given. The cylinder is illuminated broadside ( $\theta = 90^\circ$ ) with a TE wave. The absolute cross sections predicted by the MM/BOR and MM/BOT formulations shown in Figure 13 are in close agreement. The scattering cross sections for the foregoing cylinder with caps is depicted in Figure 14 and compared with experimental data obtained by Oshiro et al.<sup>37</sup> The inclusion of the edge region terms is critical for obtaining satisfactory results, particularly in the horizontal polarization.

The applicability of the present analysis to degenerate BOT surfaces is demonstrated in Figures 15 and 16, where the monostatic scattering cross sections for a flat plate ( $2\lambda$  on a side) and the bistatic cross section for a thin disk of  $0.8\lambda$  diameter are depicted. For the former case, the MM/BOT

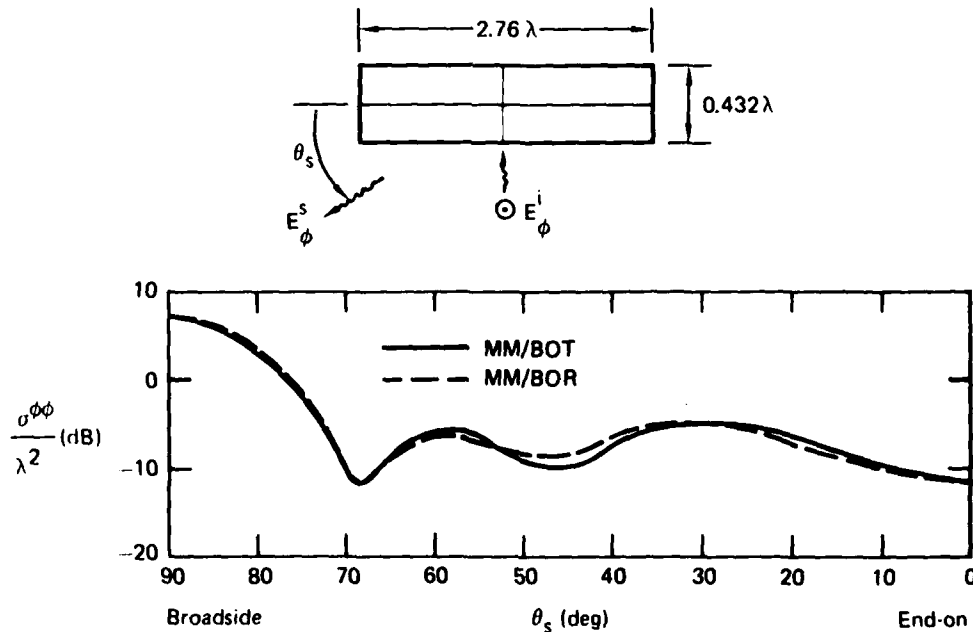


Figure 13. Comparison of MM/BOR and MM/BOT computer bistatic cross section for open cylinder: broadside illumination, TE polarization.

calculations using 4 axial modes and 16 triangle functions are compared and are in good agreement with the experimental results of Ross.<sup>34</sup> The minor discrepancies are due to the fact that the experimental data were measured for a relatively thick plate. In Figure 16, the bistatic scattering cross section for a disk is shown, comparing the MM/BOT and MM/BOR<sup>35</sup> formulations. The agreement is excellent in spite of the trapezoidal representation of the disk in the MM/BOT calculations. The disk was subdivided in the MM/BOT analysis into 24 patches.

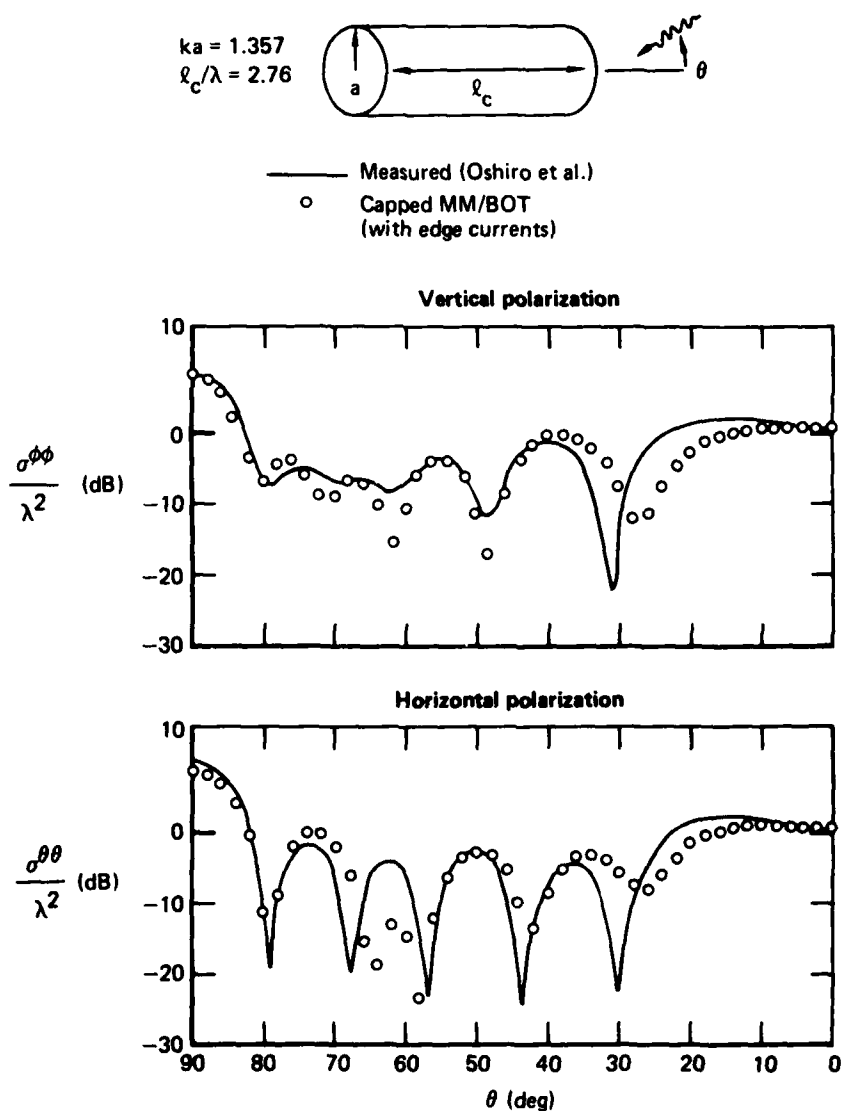


Figure 14. Measured and predicted monostatic cross section for capped cylinder.

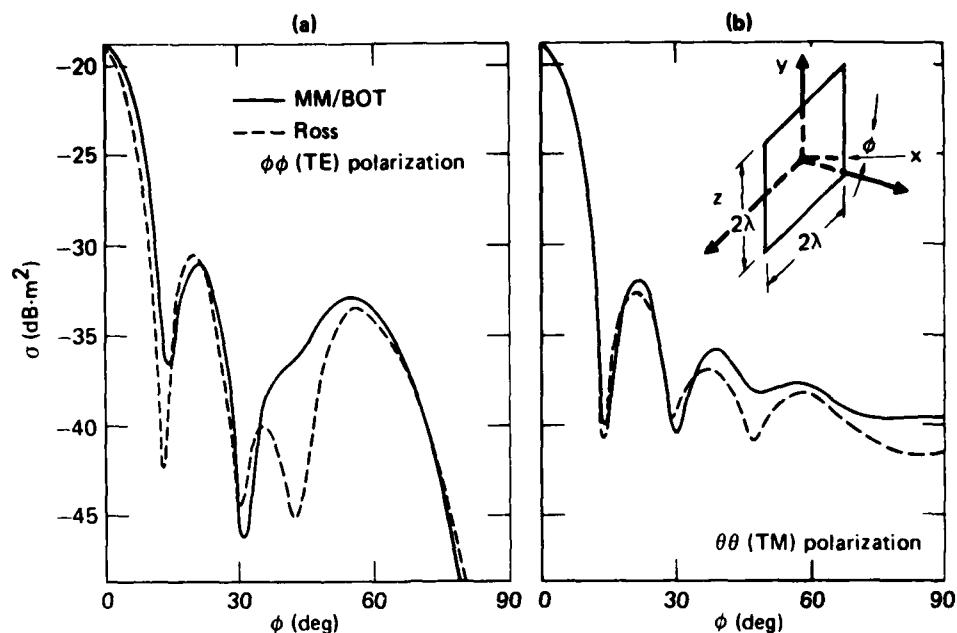


Figure 15. Monostatic scattering cross section for a square plate.

### 7.3 Validation of Near-Field Analysis

Validation of the near-field formulation for the electric and magnetic fields is shown in the subsequent examples. In this phase of the investigation, the fields were computed by the MM/BOT technique for points at distances  $\ll \lambda$  from the radiating or scattering surfaces. Unfortunately, there is a paucity of measured near-field data suitable for comparison with the present analysis. As one benchmark, the exact boundary value solution for an infinite right-circular cylinder fed with a  $\phi$ -polarized slit was used (Figure 17).<sup>36</sup> The slit subtended an angle of  $\phi_0$  deg and was excited with a uniform field. For fields sampled near the cylinder, the predictions of the MM/BOT analysis for a finite cylinder can be compared with the exact (classical) solution obtained for the infinite cylinder. A comparison of these solutions for a cylinder with  $ka = 1.35$  and a slit of  $45^\circ$  is shown in Figure 18. For the MM/BOT analysis, the cylinder length was chosen to be  $2.76\lambda$  and the slit length was  $2\lambda$ . The near fields are sampled along a line bisecting the aperture, resulting in  $E_\phi = 0$ . The closest field sampling was at  $1.2a$ , which corresponds to  $0.2a$  ( $0.04\lambda$ ) from the plane of the aperture. The calculations

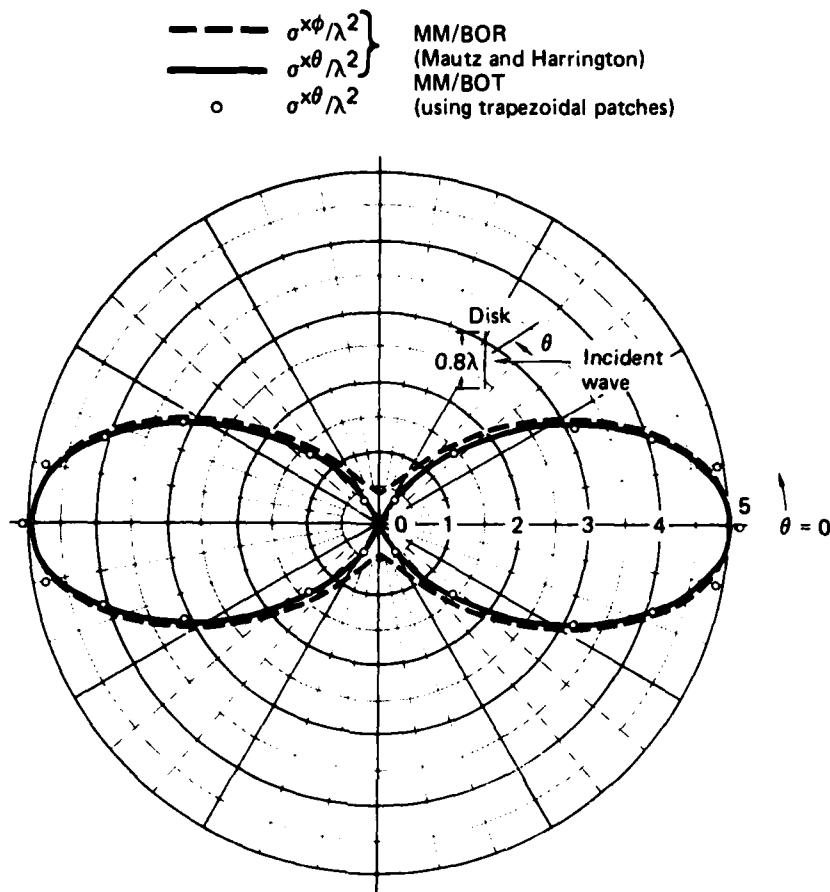
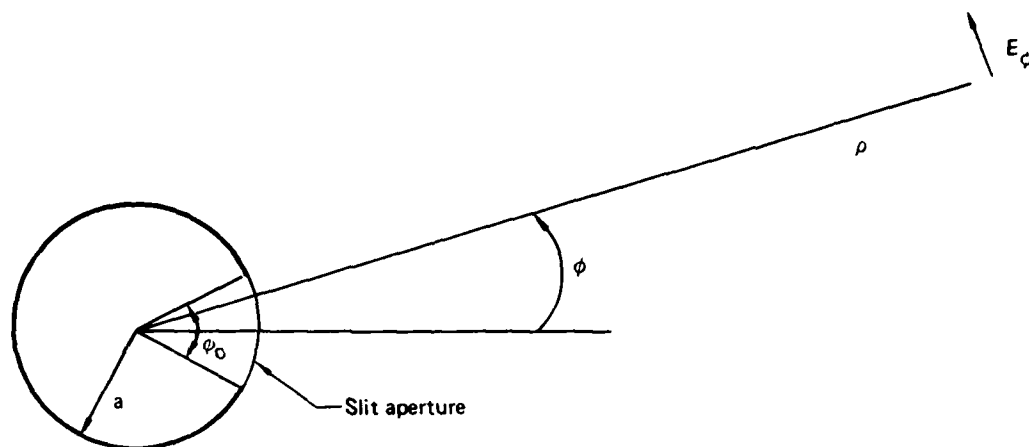


Figure 16. Comparison of MM/BOR and MM/BOT calculated bistatic cross section for a thin conducting disk;  $\sigma^{x\theta}$  = E-plane pattern,  $\sigma^{x\phi}$  = H-plane pattern.

using four and seven modes produced practically the same results. Also shown in Figure 18 are the fields obtained from a patch near-field formulation in which the sampled fields are averaged over a flat strip. The large discrepancy of the patch results from the exact solution at points near the body occurs because in this region the EM wave departs significantly from being planar. At distances  $\sim 10\lambda$ , the patch and point formulations coalesce. (As expected, at these distances, the classical solution for the infinite cylinder and the BOT results for the finite cylinder diverge.)

In Figure 19, the near-field components sampled at a radial line at  $\phi = 45^\circ$  to the aperture center are given. Again, the results of the exact and the MM/BOT solutions are in excellent agreement. The corresponding results



$$\text{Aperture field: } \begin{cases} E_0, |\phi| \leq \phi_0 \\ 0, |\phi| > \phi_0 \end{cases}$$

$$E_\phi = \frac{j\beta}{\omega\epsilon} \sum_{n=-\infty}^{\infty} b_n H_n^{(2)'}(\beta\rho) e^{jn\phi}, \beta = \frac{2\pi}{\lambda}$$

$$H_z = \sum_{n=-\infty}^{\infty} b_n H_n^{(2)}(\beta\rho) e^{jn\phi}$$

$$E_\rho = \frac{1}{j\omega\rho\epsilon} \frac{\partial H_z}{\partial \phi} \text{ where } b_n = \frac{\omega\epsilon}{j\beta} \frac{E_0}{n\pi} \sin \frac{n\phi_0}{2} \frac{1}{H_n^{(2)'}(\beta a)}$$

Figure 17. Classical solution for slit cylinder ( $\phi$ -excited slit).

for field points sampled at  $\phi = 90^\circ$  are shown in Figure 20. At sampling distances  $\gg \lambda$  from the BOT,  $E_\rho$  decreases and the EM wave front tends to become planar. In all these calculations, 4 modes were used and 17 points defined the circumference of the cylinder. As a final example, the near-field was computed for the wing configuration in Figure 12b. The result is given in Figure 21, showing the nonplanar nature of these fields. Four axial modes were used in this analysis.



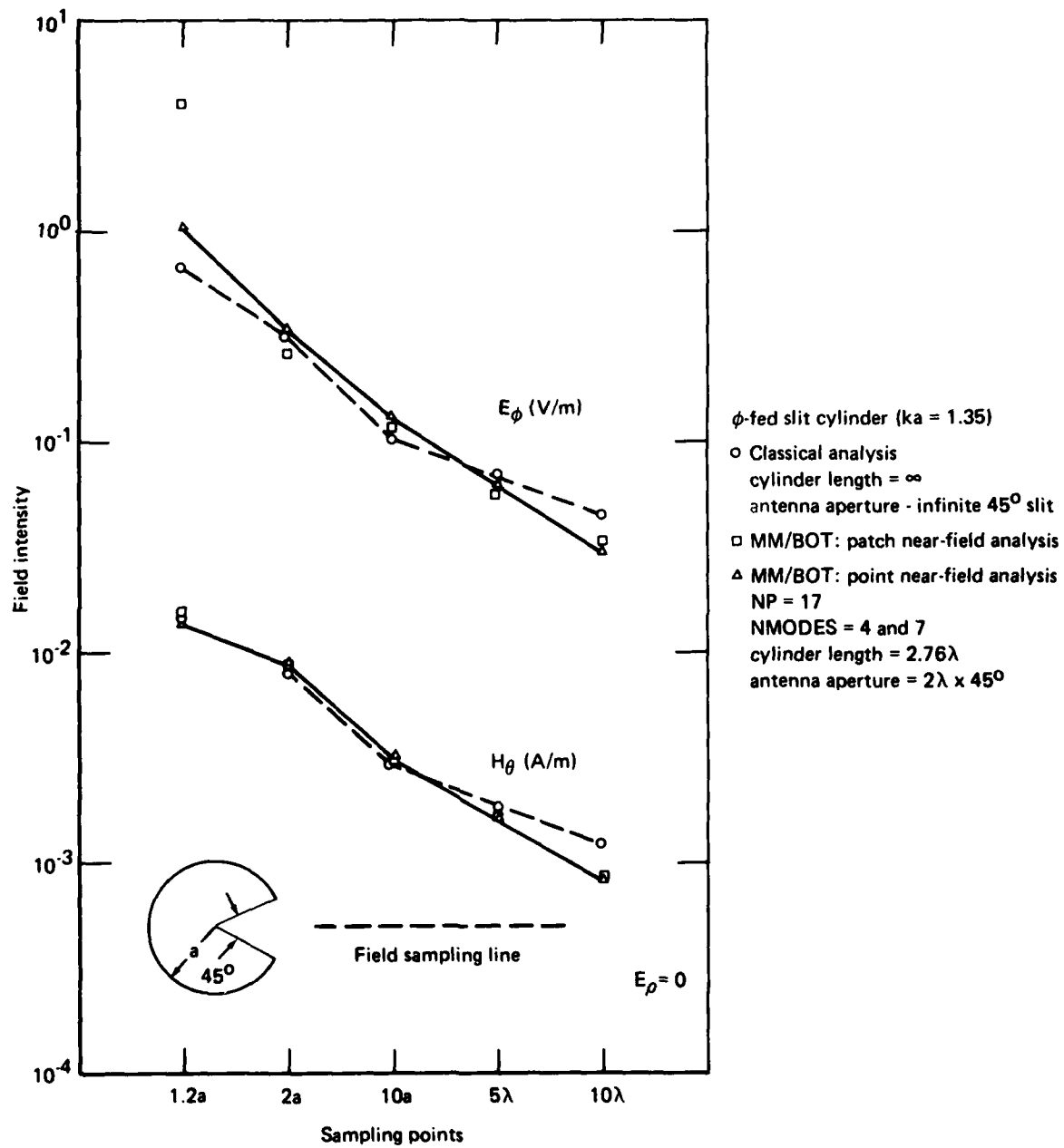


Figure 18. Computation of near fields for slit cylinder at  $\phi = 0$  (slit angle =  $45^\circ$ ).

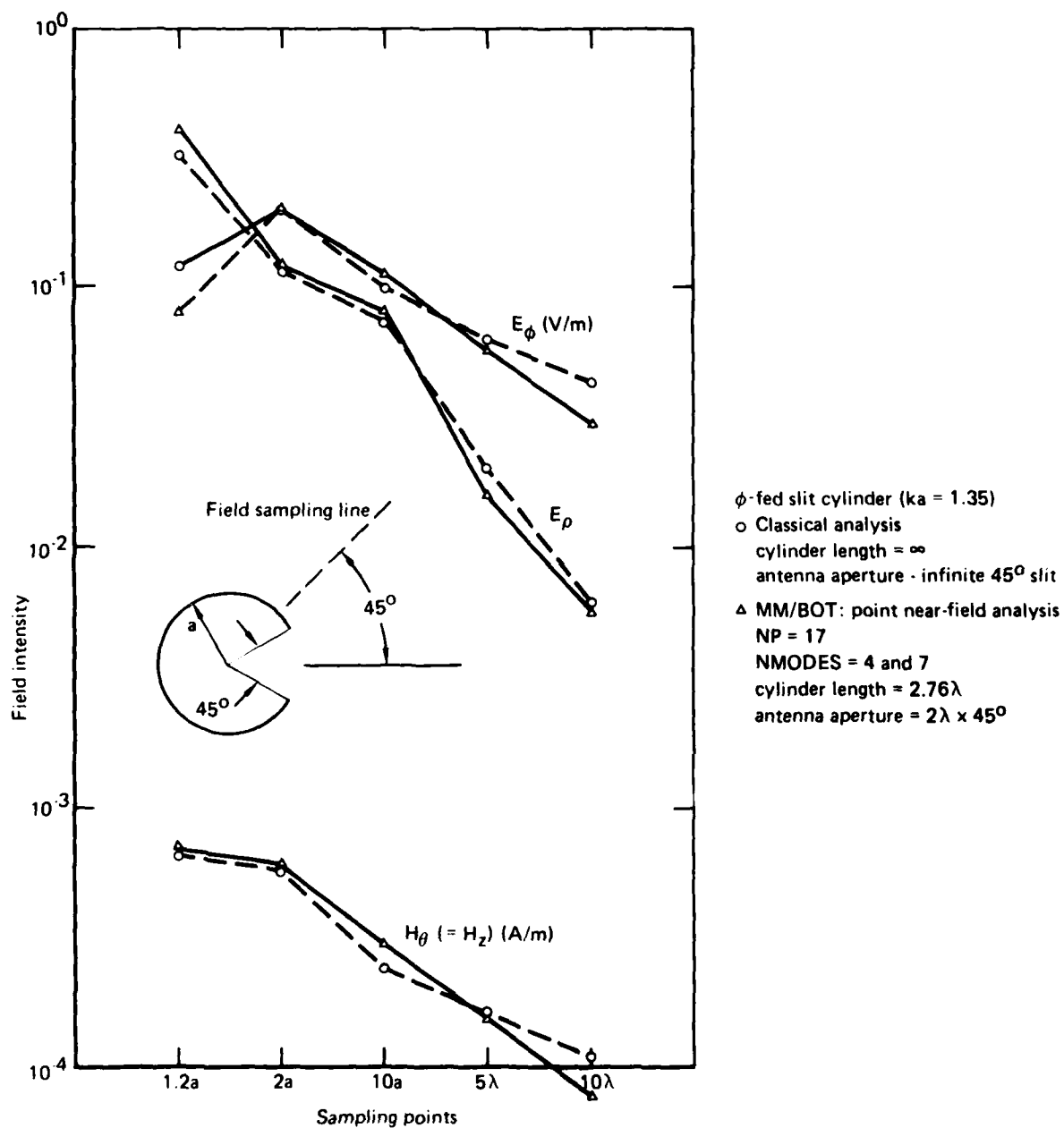


Figure 19. Computation of near fields for slit cylinder at  $\phi = 45^\circ$  (slit angle =  $45^\circ$ ).

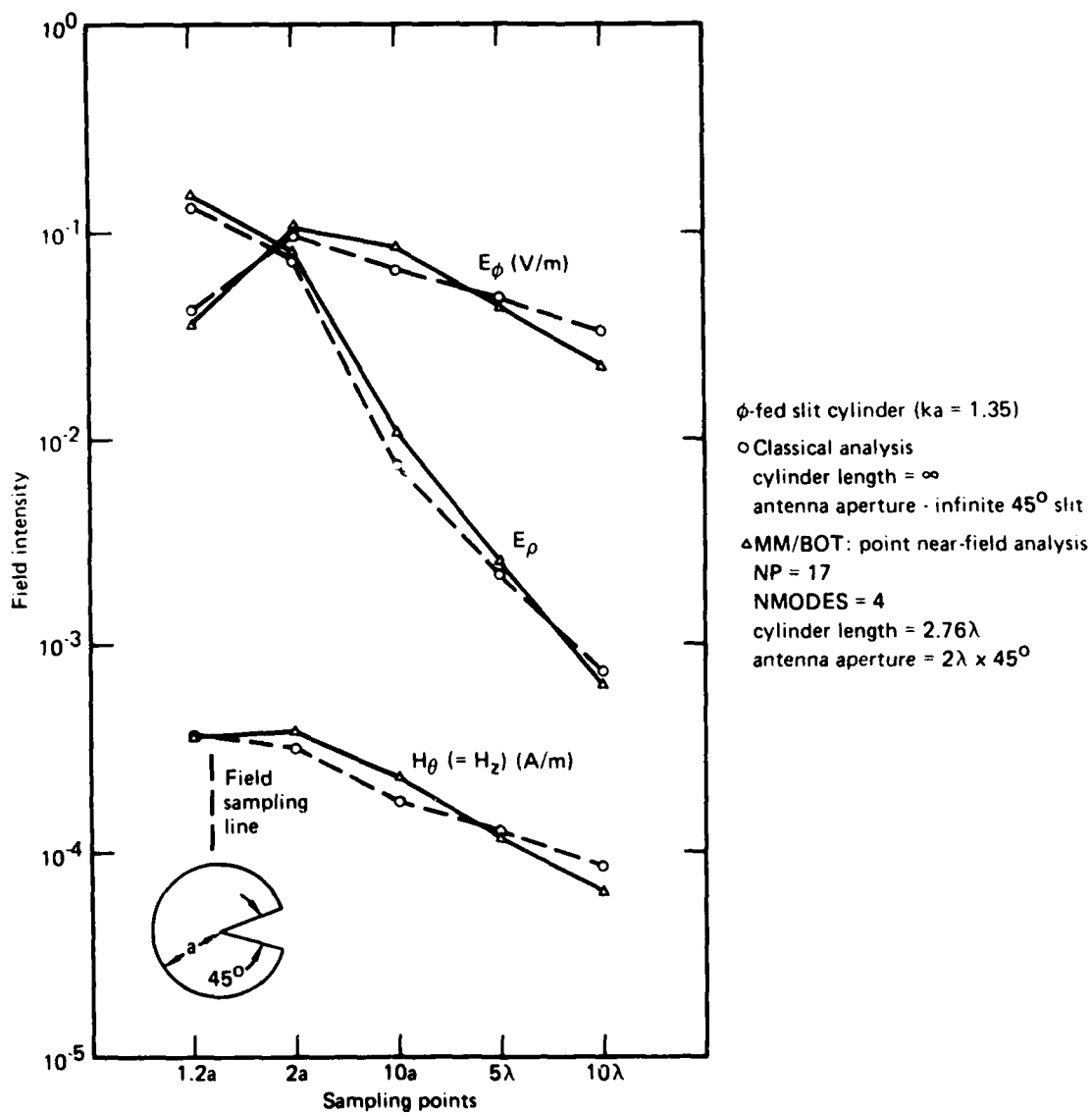


Figure 20. Computation of near fields for slit cylinder at  $\phi = 90^\circ$  (slit angle =  $45^\circ$ ).

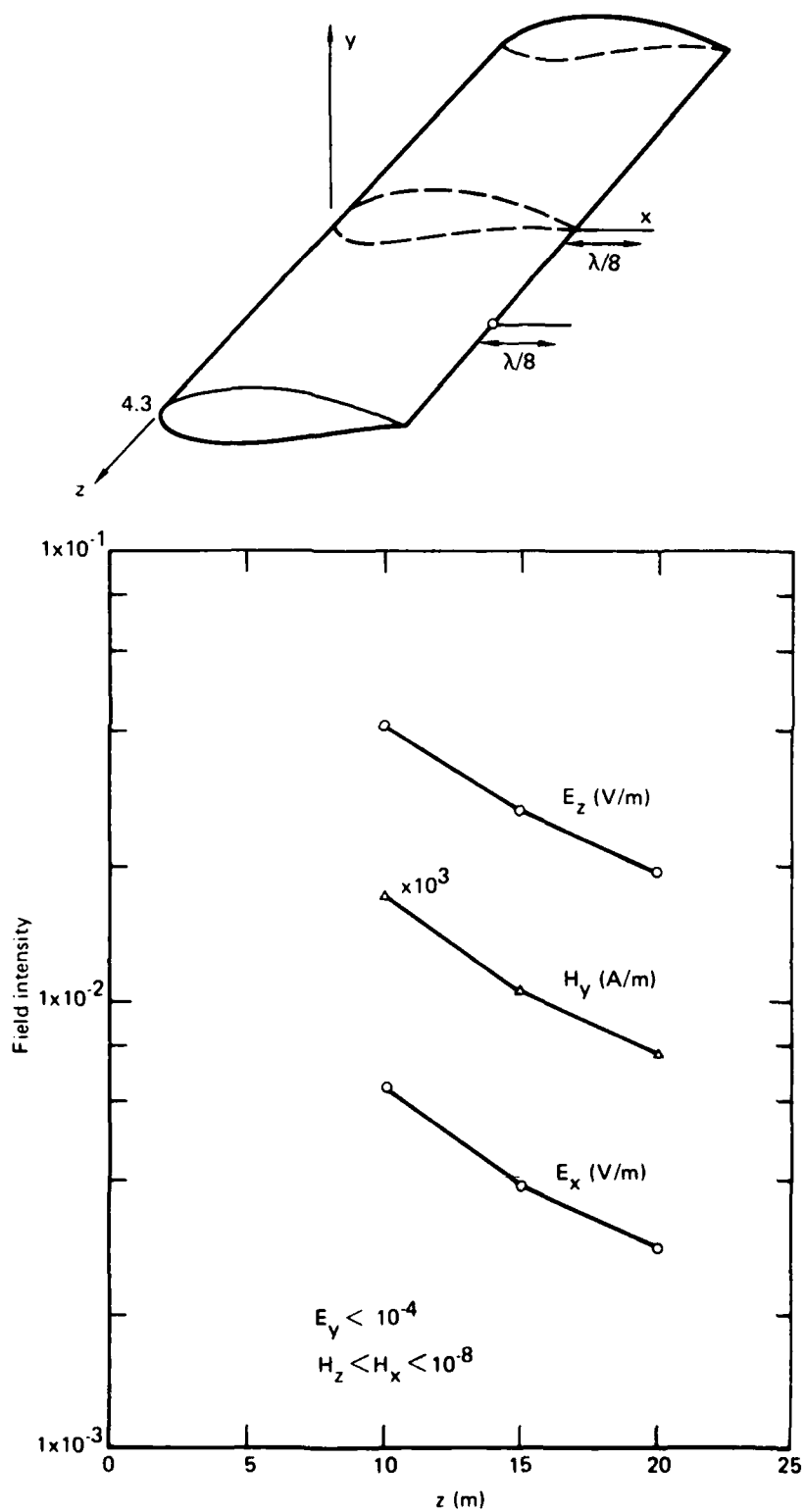


Figure 21. Near fields for wing-mounted monopoles: field sampling along z-axis.

## 8. COMPUTER IMPLEMENTATION

The MM/BOT formulation described in the preceding sections was implemented with the A-STAR computer algorithm described in detail in Volume II of this report. The overall structure of the program flow compares with that of the MM/BOR codes and the original MM/BOT code (Reference 2). The computational complexity is approximately equivalent for both MM/BOT and MM/BOR for a given size body. The matrix fill-times are comparable. The major differences lie in the fact that the modes in the present analysis do not decouple as in the MM/BOR, although, in general, the resulting network matrices remain diagonally strong and have certain symmetries. The off-diagonal submatrices for  $m \neq n$  used in the MM/BOT formulation can sometimes be deleted from the computation without excessive error penalty.

Adequate computational accuracy is achieved when the BOT surface and the wire radiators are segmented into strips  $\lesssim 0.15\lambda$  in width or length. The number of axial modes chosen is dependent upon the spatial accuracy desired for the surface currents. While the examples shown in the validation section involved mostly right-circular cylinders, the present formalism is capable of treating any asymmetric BOT, such as wing sections as is discussed in Volume II.

## APPENDIX A: DERIVATION OF THE IMPEDANCE MATRICES

The derivation of the matrix elements, contained in Equation (7) and discussed in Section 4, is detailed below.

### A.1 Impedance Matrix for the BOT Surface, $Z_{mn}^{ss}$

Using Equation (8), the elements of the partitioned submatrices of  $Z_{mn}^{ss}$  are computed from

$$\begin{aligned} (Z_{mn}^{ss, \alpha\beta})_{ij} = & \iint_{S_i} ds \iint_{S'_j} ds' jk\eta \left[ \vec{w}_{mi}^{s\alpha}(s) \cdot \vec{j}_{nj}^{s\beta}(s') \right. \\ & \left. - \frac{1}{k^2} (\nabla \cdot \vec{w}_{mi}^{s\alpha}(s)) (\nabla' \cdot \vec{j}_{nj}^{s\beta}(s')) \right] \phi, \quad (\alpha, \beta = t \text{ or } z). \end{aligned} \quad (A-1)$$

Using the expansion for  $\vec{j}^s$  (Equation (2)) and the expression for the divergence in Equation (11), and noting that  $\vec{w}_{ni}^{s\alpha} = (\vec{j}_{ni}^{s\alpha})^*$ , it can be shown that

$$\begin{aligned} (Z_{mn}^{ss, tt})_{ij} = & jk\eta \iint_{S_i} ds \iint_{S'_j} ds' [\cos(v - v') f_1^t(t) f_j^t(t') \\ & - \frac{1}{k^2} \dot{f}_1^t(t) \dot{f}_j^t(t')] v_m^{t*}(z) v_n^t(z') \phi, \end{aligned} \quad (A-2)$$

where

$$\iint_{S_i} ds = \int_L^L dz \int_1^1 dt,$$

$v$  and  $v'$  are the angles between the  $t$ -curve and the  $x$ -axis at points  $(x, y)$  and  $(x', y')$  on the BOT, respectively. Similar expressions can be obtained for the other components of  $Z_{mn}^{ss}$ . The triangle function  $f_j(\cdot)$  and its derivative  $\dot{f}_j(\cdot)$  in Equation (A-2) are approximated by four pulses, denoted as  $T_p$  and  $\dot{T}_p$ , respectively, with  $p = 1, 2, 3, 4$ , where

$$T_p = \left\{ \frac{1}{4}, \frac{3}{4}, \frac{3}{4}, \frac{1}{4} \right\} \text{ and } \dot{T}_p = \{1, 1, -1, -1\}.$$

Using the functional forms for  $v_n^t(\cdot)$  [Equation (2b)] and centroid approximating the  $t$  and  $t'$  integrals, yields

$$(Z_{mn}^{ss, tt})_{ij} \approx jk\eta \sum_{p,q=1}^4 \left\{ T_p^t T_q^t \cos(v_p - v_q) - \frac{1}{k^2} \dot{T}_p^t \dot{T}_q^t \right\} G_{mn}(p, q) \quad (A-3)$$

and similarly,

$$(Z_{mn}^{ss, tz})_{ij} \approx \frac{n\pi\eta}{kL} \sum_{p,q=1}^4 \dot{T}_p^t T_q^z G_{mn}(p, q) \quad (A-4)$$

$$(Z_{mn}^{ss, zt})_{ij} \approx -\frac{m\pi\eta}{kL} \sum_{p,q=1}^4 T_p^z \dot{T}_q^t G_{mn}(p, q) \quad (A-5)$$

$$(Z_{mn}^{ss, zz})_{ij} \approx jk\eta \sum_{p,q=1}^4 T_p^z T_q^z \left\{ \left(1 - \frac{mn\pi^2}{k^2 L^2}\right) G_{mn}(p, q) + \bar{G}_{mn}(p, q) \right\}, \quad (A-6)$$

where the function  $G_{mn}(p, q)$  is the Green's function integrated over  $ds$  and  $ds'$ , where these integrations can be carried out quasi-analytically, as discussed below, and

$$\bar{G}_{mn} = (-1)^{m+n} G_{oo} - (-1)^m G_{on} - (-1)^n G_{om}. \quad (A-6a)$$

In the above expressions, the convention, adopted in Reference 5, is used such that the indices (i,j) correspond to the indices (p,q), respectively. The corresponding triangle functions for these indexes are depicted in Figure 2b. The term  $\nu_p$  is the angle between the t-curve and the x-axis at point  $(x_p, y_p)$  on the BOT.

Evaluation of  $G_{mn}$  Functions - The evaluation of  $G_{mn}$  encompasses two surface integrals, written explicitly as

$$G_{mn}(p,q) = \int_p dt \int_q dt' \int_{-L}^L dz \int_{-L}^L dz' \exp[j\pi(-mz + nz')/L] \phi, \quad (A-7)$$

where the  $t$  and  $t'$  integrations are carried out over the  $p$  and  $q$ -th subsegments (strips) associated with the  $i$ -th and  $j$ -th axial strips on the BOT (see Figure 2b). Letting  $\xi = \frac{z - z'}{L}$ , the two integrations over  $z$  and  $z'$  reduce to

$$G_{mn}(p,q) = 4\pi L \int_0^2 d\xi u_{mn}(\xi) \int_p dt \int_q dt' \phi, \quad (A-8)$$

where

$$u_{mn}(\xi) = \begin{cases} \frac{1}{\pi} \left(1 - \frac{\xi}{2}\right) \cos n\pi\xi; & m = n \\ \frac{1}{\pi} \frac{(-1)^{m-n+1}}{(n-m)\pi} \sin\left(\frac{n-m}{2}\right) \pi\xi \cos\left(\frac{n+m}{2}\right) \pi\xi; & m \neq n \end{cases} \quad (A-9)$$

and

$$\phi = \frac{1}{4\pi R} \exp(-jKR), \quad (A-10)$$



$$R = \sqrt{\frac{\rho^2}{L^2} + \xi^2}, \quad \rho^2 = (x - x')^2 + (y - y')^2, \quad \text{and } K = kL.$$

Evaluating the integrals over  $t$  and  $t'$  by centroid approximation over the intervals  $\Delta t_p$  and  $\Delta t_q$  yields

$$G_{mn}(p, q) = L \int_0^2 d\xi u_{mn}(\xi) (\Delta t_p) (\Delta t_q) \frac{e^{-jKR_{pq}}}{R_{pq}}, \quad (\text{A-11})$$

where  $R_{pq}$  is obtained by evaluating  $\rho$  at  $\rho_{pq}$ , i.e.,

$$\rho_{pq} = \sqrt{(x_p - x_q)^2 + (y_p - y_q)^2}.$$

An alternate evaluation of Equation (A-8) can be carried out by using a Taylor-expansion about  $t_p$  and approximating the resulting integral by a series as is done in Reference 5. The present procedure is computationally more streamlined than the former.

For the self-terms (i.e.,  $\rho_{pq} = 0$ ), Equation (A-7) reduces to the form,

$$G_{mn} = 2L^2 \int_0^2 d\xi u_{mn}(\xi) e^{-jK\xi} \left\{ -jK \frac{\Delta t_q}{2L} + (1 + jK\xi) \left[ \ln \left( \frac{\Delta t_q}{2L} + \sqrt{\left( \frac{\Delta t_q}{2L} \right)^2 + \xi^2} \right) - \ln \xi \right] \right\} \quad (\text{A-12})$$

The integral over  $\xi$  can be evaluated numerically via Gaussian quadrature or a Simpson integration routine after an integration by parts is used to soften the  $\ln \xi$  singularity at the lower limit. Thus,

$$G_{mn} = 2L^2 \int_0^2 d\xi e^{-jK\xi} \left\{ u_{mn}(\xi) \left[ -jK \frac{\Delta t}{2L} + (1 + jK\xi) \ln \left( \frac{\Delta t}{2L} + \sqrt{\left( \frac{\Delta t}{2L} \right)^2 + \xi^2} \right) \right. \right. \\ \left. \left. - jK\xi(2 \ln \xi - 1) \right] + \xi (\ln \xi - 1) u'_{mn}(\xi) \right\}. \quad (A-13)$$

#### A.2 Impedance Matrix for the Caps, $Z^{cc}$

Specializing Equation (8) for the caps yields

$$Z_{kl}^{cc, \alpha\beta} = jk\eta \iint_{S_k} ds \iint_{S'_l} ds' \left\{ \vec{w}_k^{c\alpha} \cdot \vec{j}_l^{c\beta} - \frac{1}{k^2} (\nabla \cdot \vec{w}_k^{c\alpha}) (\nabla' \cdot \vec{j}_l^{c\beta}) \right\} \phi_{kl}, \\ [\alpha, \beta = t \text{ or } \rho (= \text{polar coordinate})] \quad (A-14)$$

where the surface integrals are over the  $k$  and  $l$ -th patches. Using Equations (3) and (14), we obtain

$$Z_{kl}^{cc, tt} = jk\eta \iint_{S_k} ds \iint_{S'_l} ds' \left\{ \cos(v - v') f_k^t f_l^t g_k^t g_l^t \right. \\ \left. - \frac{1}{k^2 \rho_k \rho_l} \dot{f}_k^t \dot{f}_l^t g_k^t g_l^t \right\} \phi_{kl}. \quad (A-15)$$

(The independent variables  $t$  and  $\rho$  are suppressed in  $f$  and  $g$  for notational simplicity.) The integrals in Equation (A-15) can be evaluated using a four-pulse representation for the triangle functions  $f_k$  and  $g_k$ , denoted by  $f_p$  and  $g_p$ , yielding

$$Z_{kl}^{cc,tt} \approx jk\eta \sum_{p,q=1}^{16} \left\{ \cos(\nu_p - \nu_q) f_p^t f_q^t - \frac{1}{k^2 \rho_p \rho_q} \dot{f}_p^t \dot{f}_q^t \right\} g_p^t g_q^t G_{pq}, \quad (A-16a)$$

where  $G_{pq}$  denotes the integrated free-space Green's function over the trapezoidal areas subtended by the p-th and q-th pulses and corresponding to the k-th and l-th patches, respectively. Similarly,

$$Z_{kl}^{cc,\rho t} \approx jk\eta \sum_{p,q=1}^{16} \left\{ \cos(\phi_p - \nu_q) f_p^\rho g_p^\rho f_q^t g_q^t - \frac{1}{k^2 \rho_q} f_p^\rho \hat{g}_p^\rho \dot{f}_q^t g_q^t \right\} G_{pq}, \quad (A-16b)$$

where

$$\hat{g}_p^\rho = (\bar{r}_p)^{-1} \dot{g}_p^\rho + r_p^{-1} g_p^\rho,$$

$$Z_{kl}^{cc,t\rho} = Z_{lk}^{cc,\rho t}, \quad (A-16c)$$

and

$$Z_{kl}^{cc,\rho\rho} \approx jk\eta \sum_{p,q=1}^{16} \left\{ \cos(\phi_p - \phi_q) f_p^\rho g_p^\rho f_q^\rho g_q^\rho - \frac{1}{k^2} f_p^\rho f_q^\rho \hat{g}_p^\rho \hat{g}_q^\rho \right\} G_{pq}. \quad (A-16d)$$

For the nonself term case,  $k \neq l$ ,

$$G_{pq} = A_p A_q \phi_{pq}, \quad (A-17a)$$

where  $A_p$  and  $A_q$  are the trapezoidal areas subtended by p-th and q-th pulses, and  $\phi_{pq}$  is the Green's function evaluated at the center of each area. For the self-terms,  $k = l$  or  $p = q$ ,  $G_{pp}$  is evaluated by carrying out the integration over a given trapezoidal patch shown in Figure 3, yielding

$$\begin{aligned}
G_{pp} &\approx \frac{1}{4\pi} \int_{r_1}^{r_2} r dr \int_{r_1}^{r_2} r' dr' \int_{-\theta_1}^{\theta_1} d\theta d\theta' \frac{e^{-jk\sqrt{r^2 + (r')^2 - 2rr' \cos(\theta - \theta')}}}{\sqrt{r^2 + (r')^2 - 2rr' \cos(\theta - \theta')}} \\
&\approx \frac{(r_1 + r_2)}{2\pi} (r_2 - r_1) \theta_1^2 \int_{r_1}^{r_2} r dr \frac{e^{-jk\sqrt{\bar{r}^2 + r^2 - 2r\bar{r} \cos \theta_1}}}{\sqrt{\bar{r}^2 + r^2 - 2r\bar{r} \cos \theta_1}} \quad (A-17b)
\end{aligned}$$

where  $\bar{r} = \frac{1}{2} (r_1 + r_2)$ . The last integration is done numerically.

### A.3 Impedance Matrix for the BOT-cap Interactions, $Z_m^{sc}$

For this case, Equation (8) becomes

$$(Z_m^{sc, \alpha\beta})_{i\ell} = jk\eta \iint_{S_i} ds \iint_{S'_\ell} ds' \left\{ \vec{W}_{mi}^{s\alpha} \cdot \vec{J}_\ell^{c\beta} - \frac{1}{k^2} (\nabla \cdot \vec{W}_{mi}^{s\beta}) (\nabla' \cdot \vec{J}_\ell^{c\alpha}) \right\} \Phi,$$

$$(\alpha = t \text{ or } z; \beta = t \text{ or } \rho)$$

(A-18)

where  $S_i$  and  $S'_\ell$  denote the  $i$ -th axial strip on the BOT and  $\ell$ -th patch on the caps, respectively. Using Equations (2) and (3) for the current expansions and Equations (11) and (14) for the divergence terms and noting that  $\vec{W}_{mi}^{s\alpha} = (\vec{J}_{mi}^{s\alpha})^*$ , Equation (A-18) can be written explicitly as

$$(Z_m^{sc, tt})_{i\ell} = jk\eta \iint_{S_i} ds \iint_{S'_\ell} ds' \left\{ \cos(v - v') f_i^t v_m^{t*} f_\ell^t g_\ell^t \right\}$$

$$- \frac{1}{k^2 \rho_\ell} \left\{ \dot{f}_i^t v_m^{t*} \dot{f}_\ell^t g_\ell^t \right\} \phi . \quad (\text{A-19})$$

(The independent variables in the  $f$ ,  $g$ , and  $v$  functions are implied.) As in Sections A.1 and A.2, using pulse approximations for the  $f$  and  $g$  functions on both the BOT strip and the cap patch, yields

$$(Z_m^{sc,tt})_{i\ell} = jk\eta \sum_{p=1}^4 \sum_{q=1}^{16} \left\{ \cos(v_p - v_q) T_p^t f_q^t - \frac{1}{k^2 \rho_q} \dot{T}_p^t \dot{f}_q^t \right\} g_q^t G_m(p, q) \quad (\text{A-20a})$$

and similarly,

$$(Z_m^{sc,zt})_{i\ell} = - \frac{m\pi\eta}{kL} \sum_{p=1}^4 \sum_{q=1}^{16} T_p^z \dot{f}_q^t g_q^t \rho_q^{-1} G_m(p, q) \quad (\text{A-20b})$$

$$(Z_m^{sc,tp})_{i\ell} = jk\eta \sum_{p=1}^4 \sum_{q=1}^{16} \left\{ \cos(v_p - \phi_q) T_p^t g_q^\rho - \frac{1}{k^2} \dot{T}_p^t \hat{g}_q^\rho \right\} f_q^\rho G_m(p, q) \quad (\text{A-20c})$$

$$(Z_m^{sc,zp})_{i\ell} = \frac{-m\pi\eta}{kL} \sum_{p=1}^4 \sum_{q=1}^{16} T_p^z f_q^\rho \hat{g}_q^\rho G_m(p, q) , \quad (\text{A-20d})$$

where

$$G_m(p, q) = \Delta t_p A_q \int_{-L}^L dz \exp(-jm\pi z/L) \phi_{pq}(z) \quad (\text{A-21})$$

and

$$\phi_{pq}(z) = (4\pi R_{pq})^{-1} \exp(-jkR_{pq})$$

$$R_{pq} = \sqrt{(x_p - x_q)^2 + (y_p - y_q)^2 + (z - z_q)^2}.$$

$G_m(p, q)$  is evaluated by numerical integration.

#### A.4 Impedance Matrix for the BOT-Wire Interactions, $Z_m^{sw}$

In this case Equation (8) becomes

$$(Z_m^{sw, \alpha})_{i\ell} = jk\eta \iint_{S_i} ds \int_{\ell} dh' \left\{ \vec{w}_{mi}^{s\alpha} \cdot \vec{j}_{\ell}^w - \frac{1}{k^2} (\nabla \cdot \vec{w}_{mi}^{s\alpha}) \frac{dJ_{\ell}^w}{dh'} \right\} \phi, \quad (\alpha = t \text{ or } z)$$

(A-22)

where the integrals are over the  $i$ -th BOT strip and the  $\ell$ -th wire segment, the latter being a line integral. Substituting the appropriate testing and expansion functions into Equation (A-22) yields

$$(Z_m^{sw, t})_{i\ell} = jk\eta \iint_{S_i} ds \int_{\ell} dh' \left\{ \vec{u}_t \cdot \vec{u}_{\ell} f_1^t(t) f_{\ell}^w(h') - \frac{1}{k^2} \dot{f}_1^t(t) \dot{f}_{\ell}^w(h') \right\} v_m^{t*}(z) \phi,$$

(A-23)

where  $\vec{u}_{\ell}$  is a unit vector along the  $\ell$ -th wire segment. Using pulse approximations for the triangle functions on the BOT strip and wire segments,

$$(Z_m^{sw,t})_{il} = jk\eta \sum_{p,r=1}^4 \left\{ \frac{(\Delta x_r \cos \nu_p + \Delta y_r \sin \nu_p)}{\Delta l_r} T_p^t T_r - \frac{1}{k^2} \hat{T}_p^t \hat{T}_r \right\} G_m(p,r)$$

(A-24a)

and likewise,

$$(Z_m^{sw,z})_{il} = j\eta k \sum_{p,r=1}^4 \left\{ \frac{\Delta z_r}{\Delta l_r} T_p^z T_r \left[ G_m(p,r) - (-1)^m G_o(p,r) \right] + \frac{j\eta\pi}{k^2 L} T_p^z \hat{T}_r G_m(p,r) \right\},$$

(A-24b)

where  $G_m(p,r)$  is defined in Equation (A-21) where the index  $r$  is associated with the  $\ell$ -th wire segment and  $A_q \rightarrow \Delta l_r$ .

#### A.5 Impedance Matrix for the Cap-Wire Interactions, $Z^{cw}$

The elements of  $Z^{cw}$  are given by:

$$Z_{kl}^{cw,\alpha} = jk\eta \iint_{S_k} ds \int_{\ell} dh' \left\{ \hat{w}_k^{c\alpha} \cdot \hat{j}_\ell^w - \frac{1}{k^2} (\nabla \cdot \hat{w}_k^{c\alpha}) \frac{dJ_\ell^w}{dh'} \right\} \phi, \quad (\alpha = t \text{ or } \rho) \quad (A-25)$$

where the integrals are over the  $k$ -th cap patch and the  $\ell$ -th wire segment. Substituting the testing and expansion functions into Equations (A-25) and using a pulse representation for the triangle functions on the caps and the wire yields

$$Z_{kl}^{cw,t} = j\eta k \sum_{p=1}^{16} \sum_{r=1}^4 A_p \Delta \ell_r \left\{ \frac{(\Delta x_r \cos \nu_p + \Delta y_r \sin \nu_p)}{\Delta \ell_r} f_p^t g_p^t T_r - \frac{1}{k^2 \rho_p} \hat{f}_p^t g_p^t \hat{T}_r \right\} \phi_{pr} \quad (A-26a)$$

$$Z_{kl}^{cw,\rho} = j\eta k \sum_{p=1}^{16} \sum_{r=1}^4 A_p \Delta \ell_r \left\{ \frac{(\Delta x_r \cos \phi_p + \Delta y_r \sin \phi_p)}{\Delta \ell_r} f_p^\rho g_p^\rho T_r - \frac{1}{k^2} \hat{g}_p^\rho f_p^\rho \hat{T}_r \right\} \phi_{pr}, \quad (A-26b)$$

where  $\hat{g}_p^\rho = (\bar{r}_p)^{-1} \dot{g}_p^\rho + r_p^{-1} g_p^\rho$ ,  $A_p$  is the area of the trapezoidal patch spanned by the pulse functions on the caps, and  $\phi_{pr}$  is the free-space Green's function.

#### A.6 BOT-Junction Impedance Matrix, $Z_m^{sj}$

The BOT-junction impedance elements consist of a wire segment part (first term of Equation (23)) and a disk part. The former are identical to the BOT-wire interaction matrices (Equation (A-24)) except that the integration is over the attachment segment spanned by a half-triangle function (i.e.,  $\sum_{r=1}^2$  in Equation (A-24)). Using Equation (5b) in Equation (8), the disk part of  $Z_m^{sj}$  for the t and z components can be obtained as follows:

$$(Z_m^{sd,t})_i = \frac{j\eta k}{2\pi(b-a)} \iint_{S_i} ds \iint_{s'} ds' \left\{ \vec{u}_t \cdot \vec{u}_d f_i^t(t)(r' - b) - \frac{1}{k^2} \hat{f}_i^t(t) \right\} \frac{v_m^{t*}(z)}{r'} \phi \quad (A-27a)$$

and



$$\begin{aligned}
(z_m^{sd,z})_i &= \frac{jk\eta}{2\pi(b-a)} \iint_{S_i} ds \iint_{s'} ds' \left\{ \vec{u}_z \cdot \vec{u}_d(r' - b) v_m^{z*}(z) \right. \\
&\quad \left. - \frac{1}{k^2} \vec{v}_m^{z*}(z) \right\} \frac{f_1^z(t)}{r'} \phi, \quad (A-27b)
\end{aligned}$$

where  $S_i$  is over the  $i$ -th axial strip of the BOT and  $s'$  is over the disk region (Figure 2c), i.e.,

$$\iint_{s'} ds' = \int_0^{2\pi} d\alpha \int_a^b r' dr'.$$

Using Equation (2b) and a pulse representation for  $f$ , the foregoing integrals can be approximated as

$$(z_m^{sd,t})_i \approx \frac{jk\eta}{4} \sum_{p,q=1}^4 \left\{ \sin \alpha_q \cos(\nu_p - \nu_d) T_p^t \left( \frac{a-b}{2} \right) - \frac{1}{k^2} \vec{T}_p^t \right\} G_m(p,q) \quad (A-28a)$$

$$\begin{aligned}
(z_m^{sd,z})_i &\approx \frac{jk\eta}{4} \sum_{p,q=1}^4 \left\{ \cos \alpha_q T_p^z \frac{(a-b)}{2} (G_m(p,q) - (-1)^m G_o(p,q)) \right. \\
&\quad \left. + \frac{j\pi\eta}{k^2 L} T_p^z G_m(p,q) \right\}, \quad (A-28b)
\end{aligned}$$

where

$$G_m(p,q) = \Delta t_p \int_{-L}^L \exp(-jm\pi z/L) \phi_{pq} dz \quad (A-29)$$

$$\alpha_q = \frac{\pi}{2} (q - 1) + \frac{\pi}{4}; r_q = \frac{a + b}{2}$$

$$x_q = x_d + r_q \sin \alpha_q \cos \nu_d$$

$$y_q = y_d + r_q \sin \alpha_q \sin \nu_d$$

$$z_q = z_d + r_q \cos \alpha_q$$

and  $\phi_{pq}$  is the free-space Green's function with

$$R_{pq} = \sqrt{(x_p - x_q)^2 + (y_p - y_q)^2 + (z - z_q)^2}.$$

The integration over  $\alpha$  is treated by a centroid approximation of the integral at four equispaced angles on the disk, mid-distant between the outer and inner rims.

#### A.7 Edge-Dependent Impedance Matrices

In this section, the edge-edge, BOT-edge, cap-edge, and wire-edge impedance elements are derived.

The edge-edge elements are formally given by Equation (24). The first term on the right side of Equation (24) is identical with  $Z_{kl}^{cc, \rho\rho}$  in Equation (A-16d), except that the  $f$  functions are represented by half triangle functions  $h$ , and are denoted as  $\bar{Z}_{kl}^{c, \rho\rho}$ . The second term incorporates the edge-edge interactions on the BOT, i.e.,

$$\langle \vec{w}_k^{se}, L_e(\vec{J}_l^{se}) \rangle = j\eta k \iint_{S_k} ds \iint_{S_l} ds' \left\{ f_k h_k f_l h_l - \frac{1}{k^2} f_k \dot{h}_k f_l \dot{h}_l \right\} \phi_{kl},$$

(A-30a)

where for notational brevity, the independent variables are suppressed and the z-superscripts on f and h are implied in this discussion. Using a pulse representation for f and h,

$$\langle \vec{W}_k^{se}, L_e(\vec{J}_l^{se}) \rangle \approx j\eta k \sum_{p,q=1}^8 \Delta S_p \Delta S_q f_p h_p f_q h_q - \frac{1}{k^2} f_p \dot{h}_p f_q \dot{h}_q \phi_{pq},$$

where  $\Delta S_p = \Delta t \Delta z_p$  and  $\phi_{pq}$  is the free-space Green's function evaluated at the center of each pulse. The edge interaction between the BOT and the caps is similarly given by

$$\langle \vec{W}_k^{se}, L_e(\vec{J}_l^{ce}) \rangle \approx -\frac{j\eta}{k} \sum_{p=1}^8 \Delta S_p \sum_{q=1}^8 A_q f_p^z \dot{h}_p^z f_q^\rho \hat{h}_q^\rho \phi_{pq}, \quad (A-30b)$$

where

$$\hat{h}_q^\rho \equiv (\vec{r}_q)^{-1} \dot{h}_q^\rho + r_q^{-1} h_q^\rho.$$

Following the convention of the previous sections of the appendix, the indices (p, q) refer to (k, l), corresponding to the unprimed and primed coordinates, respectively. The edge interactions between the cap and the BOT are the transpose of Equation (A-30b). The total edge-edge interaction  $Z_{kl}^{ee}$  between the k-th and l-th segments is a sum of the foregoing expressions and  $\bar{Z}_{kl}^{cc,\rho\rho}$ .

Following the approach above, the interactions of the BOT surface with the edge region, formally given by Equation (25), can be written as

$$Z_{m,il}^{se,t} \approx \bar{Z}_{m,il}^{sc,tp} - \frac{j\eta}{k} \sum_{p=1}^4 \sum_{q=1}^8 \dot{T}_p^t f_q^z \dot{h}_q^z G_m(p,q) \quad (A-31a)$$

and

$$\begin{aligned}
Z_{m,il}^{se,\rho} \approx \bar{Z}_{m,il}^{sc,z\rho} + jk\eta \sum_{p=1}^4 \sum_{q=1}^8 \left\{ -T_p^z f_q^z h_q^z (-1)^m G_o(p, q) \right. \\
\left. + T_p^z f_q^z (h_q^z + \frac{j\eta\pi}{k^2 L} \dot{h}_q^z) \right\} G_m(p, q) , \quad (A-31b)
\end{aligned}$$

where

$$G_m(p, q) = \Delta S_p \Delta z_q \int_{-L}^L dz e^{-jm\pi z/L} \phi_{pq}(z)$$

and  $\phi_{pq}(z)$  is the free-space Green's function with  $R_{pq}(z) = \{(x_p - x_q)^2 + (y_p - y_q)^2 + (z - z_q)^2\}^{1/2}$ .

Similarly, the interactions of the cap surface with the edge region, given in Equation (26), can be written explicitly as

$$Z_{kl}^{ce,t} \approx \bar{Z}_{kl}^{cc,tp} + \frac{j\eta}{k} \sum_{p=1}^{16} A_p \sum_{q=1}^8 \Delta S_q \rho_p^{-1} \dot{T}_p^t g_p^t f_q^z \dot{h}_q^z \phi_{pq} \quad (A-32a)$$

and

$$Z_{kl}^{ce,\rho} \approx \bar{Z}_{kl}^{cc,\rho\rho} + \frac{j\eta}{k} \sum_{p=1}^{16} A_p \sum_{q=1}^8 \Delta S_q (\hat{g}_p^\rho f_p^\rho f_q^z \dot{h}_q^z) \phi_{pq} , \quad (A-32b)$$

where  $\hat{g}_p^\rho$  is defined as  $\hat{h}_p^\rho$  before.

Finally, the wire (radiator)-edge interactions between the  $i$ -th radiator and the  $j$ -th edge segments, in Equation (27), can be written in terms of pulse representations of the triangle functions as

$$\begin{aligned}
Z_{ij}^{we} = & \bar{Z}_{ij}^{wc,t} + j\eta k \sum_{p=1}^4 \sum_{q=1}^8 \Delta \ell_p \Delta S_q \left\{ (\vec{u}_\ell \cdot \vec{u}_z') f_p^w h_q^z \right. \\
& \left. - \frac{1}{k^2} \vec{f}_p^w \cdot \vec{h}_q^z f_q^z \right\} \phi_{pq} .
\end{aligned}
\tag{A-33}$$

# REFERENCES

1. B. J. Strait (Editor), Applications of the Method of Moments to Electromagnetic Fields (SCEEE Press, Syracuse, 1981).
2. L. N. Medgyesi-Mitschang, Radiation and Scattering from Bodies of Translation, RADC Report TR-80-142 (Vol. I), April 1980. (A087402)
3. J. F. Shaeffer and L. N. Medgyesi-Mitschang, Radiation from Wire Antennas Attached to Bodies of Revolution: The Junction Problem, *IEEE Trans. Antennas Propagat.* AP-29, 479 (1981).
4. R. Mittra (Editor), Computer Techniques for Electromagnetics (Pergamon Press, New York, 1973).
5. J. R. Mautz and R. F. Harrington, Radiation and Scattering from Bodies of Revolution, *Appl. Sci. Res.* 20, 405 (1969).
6. G. J. Burke and A. J. Poggio, Numerical Electromagnetics Code-Method of Moments, AFWL-TR-76-320, July 1977.
7. R. F. Harrington, Field Computation by Moment Methods, (Macmillan Company, New York, 1968).
8. R. F. Harrington, Matrix Methods for Field Problems, *Proc. IEEE* 55, 136 (1967).
9. N. C. Albertsen, J. E. Hansen, and N. E. Jensen, Computation of Radiation from Wire Antennas on Conducting Bodies, *IEEE Trans. Antennas Propagat.* AP-22, 200 (1974).
10. N. C. Albertsen, J. E. Hansen, and N. E. Jensen, Computation of Spacecraft Antenna Radiation Patterns, European Space Research Organization ESRO CR-207, Sept. 1973.
11. J. R. Mautz, Scattering from Loaded Wire Objects Near a Loaded Surface of Revolution, Syracuse University Research Corporation, SURC TN 74-030, Jan. 1974.
12. E. H. Newman and D. M. Pozar, Electromagnetic Modeling of Composite Wire and Surface Geometries, *IEEE Trans. Antennas Propagat.* AP-26, 784 (1978).
13. E. H. Newman and D. M. Pozar, Considerations for Efficient Wire/Surface Modeling, *IEEE Trans. Antennas Propagat.* AP-28, 121 (1980).
14. M. N. I. Fahmy and A. Z. Botros, Radiation from Quarter-Wavelength Monopoles on Finite Cylindrical, Conical, and Rocket-Shaped Conducting Bodies, *IEEE Trans. Antennas. Propagat.* AP-27, 615 (1979).

15. A. W. Glisson and C. M. Butler, Analysis of a Wire Antenna in the Presence of a Body of Revolution, IEEE Trans. Antennas Propagat. AP-28, 604 (1980).
16. J. H. Richmond, A Wire-Grid Model for Scattering by Conducting Bodies, IEEE Trans. Antennas Propagat. AP-14, 782 (1966).
17. J. F. Shaeffer, EM Scattering from Bodies of Revolution with Attached Wires, IEEE Trans. Antennas Propagat. (in press).
18. M. G. Andreasen, Scattering from Parallel Metallic Cylinders with Arbitrary Cross Sections, IEEE Trans. Antennas Propagat. AP-12, 746 (1964).
19. R. F. Wallenberg and R. F. Harrington, Radiation from Apertures in Conducting Cylinders of Arbitrary Cross Sections, IEEE Trans. Antennas Propagat. AP-17, 56 (1969).
20. D. R. Wilton and R. Mittra, New Numerical Approach to the Calculation of EM Scattering Properties of Two-Dimensional Bodies of Arbitrary Cross Sections, IEEE Trans. Antennas Propagat. AP-20, 310 (1972).
21. P. Ya. Ufimtsev, Diffraction of Plane Electromagnetic Waves by a Thin Cylindrical Conductor, Radiotekhnika i Elektronika, 7, 241 (1962).
22. R. B. Kiebert, Scattering by a Finite Cylinder, in Electromagnetic Theory and Antennas, Part 1, E. C. Jordan, Ed. (Pergamon Press, New York, 1963), pp. 145-156.
23. A. T. Fialkovskii, Scattering of Plane Electromagnetic Waves by a Thin, Cylindrical Conductor of Finite Length, Soviet Phys.-Tech. Phys. 11, 1300-1304.
24. A. W. Adey, Scattering of Electromagnetic Waves by Long Cylinders, Electronic Radio Eng. 149 (1958).
25. W. E. Williams, Diffraction by a Cylinder of Finite Length, Proc. Cambridge Phil. Soc. 52, 322 (1956).
26. C. C. Kao, Three-Dimensional Electromagnetic Scattering from a Circular Tube of Finite Length, J. Appl. Phys. 40, 4732 (1969).
27. C. C. Kao, Electromagnetic Scattering from a Finite Tubular Cylinder: Numerical Solutions, Radio Sci. 5, 617 (1970).
28. W. A. Davis and R. Mittra, A New Approach to the Thin Scatterer Problem Using the Hybrid Equation, IEEE Proc. Antennas Propagat. AP-25, 402 (1977).

29. A. W. Glisson and D. R. Wilton, Simple and Efficient Numerical Methods for Problems of Electromagnetic Radiation and Scattering from Surfaces, IEEE Trans. Antennas Propagat. AP-28, 593 (1980).
30. J. J. H. Wang, Numerical Analysis of Three-Dimensional Arbitrarily-Shaped Conducting Scatterers by Trilateral Surface Cell Modeling, Radio Sci. 13, 947 (1978).
31. R. M. Bevensee, The Syracuse Computer Code for Radiation and Scattering from Bodies of Revolution, Extended for Near-Field Computations, Lawrence Livermore Laboratory Report UCRL-51622 (May 1974).
32. L. N. Medgyesi-Mitschang and J. H. Mullen, Radiation and Scattering from Asymmetrically Excited Bodies of Revolution, IEEE Trans. Antennas Propagat. AP-24, 90, (1976).
33. L. N. Medgyesi-Mitschang and J. M. Putnam, User's Guide for COBRRA: Codes for Body-of-Revolution/Radiator Analysis, McDonnell Douglas MDC Q0644, December 1977.
34. R. A. Ross, Radar Cross Section of Rectangular Flat Plates as a Function of Aspect Angle, IEEE Trans. Antennas Propagat. AP-14, 329 (1966).
35. R. F. Harrington and J. R. Mautz, Radiation and Scattering from Bodies of Revolution, Final Report, AFCRL-69-0305, July 1969.
36. E. C. Jordan, Electromagnetic Waves and Radiating Systems (Prentice-Hall, Inc., 1950), p. 587.
37. F. K. Oshiro, K. M. Mitzner, and S. S. Locus, Calculation of Radar Cross Sections, Technical Report AFAL-TR-70-21, 1970.



DATE  
FILMED  
— 8